
A CLASS OF MODULAR AND FLEXIBLE COVARIATE-BASED COVARIANCE FUNCTIONS FOR NONSTATIONARY SPATIAL MODELING

A PREPRINT

 **Federico Blasi**

Department of Mathematical
Modeling and Machine Learning
University of Zurich
Zurich, Switzerland
federico.blasi@uzh.ch

 **Reinhard Furrer**

Department of Mathematical
Modeling and Machine Learning
University of Zurich
Zurich, Switzerland
reinhard.furrer@math.uzh.ch

ABSTRACT

The assumptions of stationarity and isotropy often stated over spatial processes have not aged well during the last two decades, partly explained by the combination of computational developments and the increasing availability of high-resolution spatial data. While a plethora of approaches have been developed to relax these assumptions, it is often a costly tradeoff between flexibility and a diversity of computational challenges. In this paper, we present a class of covariance functions that relies on fixed, observable spatial information that provides a convenient tradeoff while offering an extra layer of numerical and visual representation of the flexible spatial dependencies. This model allows for separate parametric structures for different sources of nonstationarity, such as marginal standard deviation, geometric anisotropy, and smoothness. It simplifies to a Matérn covariance function in its basic form and is adaptable for large datasets, enhancing flexibility and computational efficiency. We analyze the capabilities of the presented model through simulation studies and an application to Swiss precipitation data.

Keywords covariate-based covariance function · covariance function · Gaussian process · estimation · prediction · regularization · nonstationarity · large sample size

1 Introduction

The field of applied spatial statistics has focused since its early beginnings on the challenging task of modeling spatial data with Gaussian processes, requiring a nuanced understanding of how processes vary across the domain, represented through the covariance function. Traditionally, this function was assumed to be stationary, implying consistent covariance across spatial distances, regardless of location. Yet, the rapid increase in both the quality and quantity of spatial datasets during the current century has exposed the limitations of stationary covariance functions, calling for more adaptable approaches.

Various methods have been developed to address the rigidity of covariance functions. These include convolving stationary orthogonal processes Fuentes [2001], applying deformation techniques [Sampson and Guttorp, 1992], and employing recent advancements in deep learning [Zammit-Mangion et al., 2021]. See Gelfand et al. [2010], Ch.9, Fouedjio [2017], and Schmidt and Guttorp [2020], for an overview of nonstationary approaches. In this article, we focus on the stem of nonstationary covariance functions that leverage observable spatial covariates based on the intuitive idea that deviations from stationarity can be (partially) explained by local geographic characteristics. Similar to mean regression, by conditionally modeling the variance on available covariates, we can capture the spatially-varying nature of the spatial structure of the process more effectively. It increases flexibility and computational efficiency, providing a convenient tradeoff between the two, and adds a layer of interpretability by linking changes in spatial structure to specific covariates.

The last two decades have seen considerable interest in covariate-based covariance functions. Hoef et al. [2006] developed spatial models whose covariance structures incorporate flow and stream distance through spatial moving averages. Cooley et al. [2007] modeled extreme precipitation by representing the process in the climate space, mainly composed by elevation and mean precipitation at the weather station. Calder [2008] included wind direction information from a single location in the kernel convolution approach of Higdon [1998]. Reich et al. [2011] extended the work done by Fuentes [2002], modeling the nonstationarity covariance function as a weighted sum of independent stationary zero-mean Gaussian processes, where the weights are obtained through spatially related covariate information. Schmidt et al. [2011] extended the work done by Sampson and Guttorp [1992] considering a d -dimensional space, from which $d - 2$ are related to covariates. The stationary isotropic covariance function of the extended space is modeled with a Matérn covariance function with a Mahalanobis distance that models the roughness and smoothness of the spatial process for the different directions. Another extension of [Sampson and Guttorp, 1992] is the work done by Bornn et al. [2012], who devised a method that embeds the original nonstationary field in a higher-dimensional space where it can be more straightforwardly described and modeled. It differs from the work done by Sampson and Guttorp [1992] in that here, the locations in the geographic space are retained, with added flexibility obtained through the extra dimensions related to covariates. Neto et al. [2014] modeled the covariance structure conditionally on the wind direction information for an air pollution process. This is done via the convolution approach, proposing tailored functions that include wind direction. Risser and Calder [2015] introduced a covariance function based on the nonstationary covariance model of Paciorek and Schervish [2006] that considers covariate information. Sources of nonstationarity such as the marginal standard deviation and spatial anisotropy are modeled separately with a parametric model. The focus is mainly on interpretability while preserving a low-dimensional parameterization, where the flexibility component is sensitive to the covariates and the parametric model offered. Gilani et al. [2016] presented a nonstationary spatio-temporal model for three traffic-related pollutants in a localized near-road environment, combining the nonstationary methods by Fuentes [2002] and Schmidt et al. [2011], each of them considering covariates such as distance from the main road, and wind direction, among others, driving the nonstationarity and the mixture weights. Xu and Gardoni [2018] proposed an improved latent space approach for modeling nonstationary spatial and spatiotemporal random fields. By considering regressors as latent dimensions, they characterize the nonstationarity using a regressor-based standard deviation and correlation.

While these approaches are capable of representing nonstationary spatial structures, they often involve a costly tradeoff between flexibility and computational efficiency, limiting the number and extent of different sources of nonstationarity and their applicability to large sample sizes. Costly tradeoffs will often lead to limited flexibility, with limited predictive gains, which, on top of the need for hand-crafted implementations and identifiability issues often present in these contexts, will discourage the use of nonstationary approaches in practice.

Our article presents a class of covariate-based covariance functions that provides a convenient tradeoff, by offering a flexible and economical representation of the nonstationary process, representing a wide range of key sources of nonstationarity of the spatial structure in a modular framework. It allows for separate parametric structures for different types of nonstationarity, such as variance, local anisotropy, and smoothness. Moreover, we introduce an efficient, tailored regularization approach to foster well-posed covariance matrices that attenuate potential numerical issues. It simplifies to a Matérn covariance function in its basic form and, thanks to its modularity, is adaptable for large datasets, extending the convenient tradeoff across a wide range of sample sizes.

The article is structured as follows. In Section 2, we introduce the likelihood-based framework as well as the stem of nonstationary covariance functions based on convolution, necessary roots to introduce Section 3, where we present the modular nonstationary covariance function and assess through simulation study the feasibility of model selection via classical approaches. In Section 4, we present an illustration with monthly precipitation data from Switzerland, where we also compare it to existing methodologies. Section 5 provides a discussion of the presented topic.

2 Likelihood-based approach with nonstationary covariance functions

It is of common practice to assume that the spatial variable Z defined on the study region $\mathcal{D} \subseteq \mathcal{R}^d$, can be modeled as a Gaussian process $Z(\cdot) \sim \text{GP}(\mu(\cdot), \mathcal{C}(\cdot, \cdot))$ with some mean function $\mu(\cdot)$ and covariance function $\mathcal{C}(\cdot, \cdot)$. Considering \mathbf{s} as the spatial location, a typical decomposition of $Z(\cdot)$ is then given by

$$Z(\mathbf{s}) = \mu(\mathbf{s}) + Y(\mathbf{s}) + \epsilon(\mathbf{s}), \quad \mathbf{s} \in \mathcal{D}, \quad (1)$$

where $Y(\cdot)$ is a zero-mean smooth Gaussian process representing the spatial dependencies, and a third component is often considered to describe the measurement error and micro-scale variability, represented as a Gaussian random noise process $\epsilon(\cdot)$ with mean zero and variance σ_ϵ^2 , independent of $Y(\cdot)$. Our sample $\mathbf{z} = (z_1, \dots, z_n)^\top$ is the result of observing $Z(\cdot)$ at mutually distinct sampling locations $\{\mathbf{s}_1, \dots, \mathbf{s}_n\}$, i.e., observing a multivariate Gaussian distribution $\{Z(\mathbf{s}_1), \dots, Z(\mathbf{s}_n)\} \sim \mathcal{N}_n(\boldsymbol{\mu}, \boldsymbol{\Sigma}_Y + \mathbf{I}_n \sigma_\epsilon^2)$, being $\boldsymbol{\mu}$ a $n \times 1$ vector of elements $\mu(\mathbf{s}_\ell)$, $\boldsymbol{\Sigma}_Y$ a $n \times n$ symmetric positive

semi-definite matrix with elements $[\Sigma_Y]_{i,j} = \mathcal{C}(\mathbf{s}_i, \mathbf{s}_j)$, and where $\mathbf{I}_n \sigma_\epsilon^2$ is the component associated with the error process $\epsilon(\cdot)$. Then, $\Sigma_Z = \Sigma_Y + \mathbf{I}_n \sigma_\epsilon^2$. For the remainder of the article, we adopt parametric forms for $\mu(\cdot)$ and $\mathcal{C}(\cdot, \cdot)$, with $\mu(\cdot; \boldsymbol{\beta})$ and $\mathcal{C}(\cdot, \cdot; \boldsymbol{\psi})$, where $\boldsymbol{\beta}$ and $\boldsymbol{\psi}$ are the associated unknown parameters, vectors of dimension $p + 1$ and m , respectively.

The covariance function $\mathcal{C}(\cdot, \cdot; \boldsymbol{\psi})$ is often chosen from one of the low-dimensional parameterization covariance functions (which we call *classical* covariance functions) that assumes that the underlying Gaussian process $Y(\cdot)$ is stationary, imposing the mean and covariance to be invariant under global shifts in \mathcal{R}^d , i.e., $\mu(\mathbf{s} + \mathbf{h}) = \mu(\mathbf{s})$ and that $\mathcal{C}(\mathbf{s}_i + \mathbf{h}, \mathbf{s}_j + \mathbf{h}; \boldsymbol{\psi}) = \mathcal{C}(\mathbf{s}_i, \mathbf{s}_j; \boldsymbol{\psi}), \forall \mathbf{h} \in \mathbb{R}^2$. Moreover, a more restrictive assumption often stated is isotropy, meaning that if $\mathcal{C}(\cdot, \cdot; \boldsymbol{\psi})$ is a function of $h = \|\mathbf{h}\|$ only, where $\|\cdot\|$ is a norm such as the Euclidean. Then, the process is said to be isotropic. Among the classical covariance functions, the Matérn family has received a lot of attention over the last two decades [Matérn, 2013],[Porcu et al., 2023], and takes the form of

$$\mathcal{C}(h; \boldsymbol{\psi}) = \sigma^2 \frac{2^{1-\nu}}{\Gamma(\nu)} \left(\sqrt{8\nu} \frac{h}{\gamma} \right)^\nu \mathcal{K}_\nu \left(\sqrt{8\nu} \frac{h}{\gamma} \right), \quad (2)$$

where $\sigma > 0, \gamma > 0, \nu > 0, \mathcal{K}_\nu(\cdot)$ is the modified Bessel function of the second kind of order ν [Abramowitz and Stegun, 1970], and $\Gamma(\cdot)$ is the gamma function. This parameterization links approximately the distance γ with a correlation of 0.1 [Lindgren et al., 2011] (which we call as the approximate effective scale). The parameter ν controls the degree of smoothness of the process, shaping the correlation structure at infinitesimal small distances. For example, Banerjee and Gelfand [2003] comment that for essentially featureless areas (i.e., flat surfaces), one would expect continuous and differentiable surfaces, whereas, for areas with irregular features such as ridges or canyons, even continuity would be inappropriate. As special cases, the Matérn covariance function approaches the Gaussian covariance model when $\nu \rightarrow \infty$ (up to a rescaling) and simplifies to the exponential covariance model when $\nu = 1/2$. This added flexibility compared to those with a fixed degree of smoothness plays a major role in producing optimal prediction maps, as discussed in [Stein, 1999]. The flexibility of classical covariance models is often extended by considering a global affine transformation of the Euclidean distance, where instead of the Euclidean distance h , we consider the affine transformation $\Delta \mathbf{s}^T A^{-1} \Delta \mathbf{s}$, with A a 2×2 symmetric non-singular matrix and $\Delta \mathbf{s} = \mathbf{s}_i - \mathbf{s}_j$. In this scenario, we say that the process is geometrically anisotropic, represented as h_A , related to the affine transformation A .

Once the parametric structures of the Gaussian process are defined, the parameters can be estimated using maximum likelihood techniques. For the remainder of the article, we adopt a classic regression setting for the trend $\mu(\mathbf{s}_\ell; \boldsymbol{\beta}) = \mathbf{x}_\ell^T \boldsymbol{\beta}$, where \mathbf{x}_ℓ^T are rows of the design matrix \mathbf{X} of dimension $n \times (p + 1)$, containing information of a set of p fixed covariates observed at locations $\{\mathbf{s}_1, \dots, \mathbf{s}_n\}$. Considering the available information \mathbf{z} , estimation of the parameter vector $\boldsymbol{\vartheta} = (\boldsymbol{\beta}^T, \boldsymbol{\psi}^T)^T \in \mathcal{R}^{p+m+1}$ is given by maximizing the log-likelihood function

$$l(\boldsymbol{\vartheta}) = -\frac{n}{2} \log(2\pi) - \frac{1}{2} \log \det \Sigma_Z - \frac{1}{2} (\mathbf{z} - \mathbf{X}\boldsymbol{\beta})^T \Sigma_Z^{-1} (\mathbf{z} - \mathbf{X}\boldsymbol{\beta}), \quad (3)$$

where a vector $\hat{\boldsymbol{\vartheta}}_{\text{ML}}$ maximizing $l(\cdot)$ is called a Maximum Likelihood estimate (MLE) and is found via numerical optimizers.

Prediction of the process $Z(\cdot)$ at new locations $\{\mathbf{s}_1^p, \dots, \mathbf{s}_k^p\}$ are done through the conditional distribution of $Z(\cdot)$ at $\{\mathbf{s}_1^p, \dots, \mathbf{s}_k^p\}$ given \mathbf{z} , which follows a multivariate Gaussian distribution defined as

$$\mathbf{Z}^p | \mathbf{Z} = \mathbf{z} \sim \mathcal{N}_k(\mathbf{X}^p \boldsymbol{\beta} + \Sigma_{\text{PZ}} \Sigma_Z^{-1} (\mathbf{z} - \mathbf{X}\boldsymbol{\beta}), \Sigma_{\text{P}} - \Sigma_{\text{PZ}} \Sigma_Z^{-1} \Sigma_{\text{PZ}}^T), \quad (4)$$

where Σ_{PZ} is a matrix of dimension $k \times n$ with elements $[\Sigma_{\text{PZ}}]_{i,j} = \mathcal{C}(\mathbf{s}_i^p, \mathbf{s}_j; \boldsymbol{\psi})$, the covariance between the process at unseen locations $\{\mathbf{s}_1^p, \dots, \mathbf{s}_k^p\}$, and the process at the observed locations, and Σ_{P} is the matrix $k \times k$ with elements $\mathcal{C}(\mathbf{s}_{0_i}, \mathbf{s}_{0_j}; \boldsymbol{\psi})$. Finally, we replace the covariance matrices with the maximum likelihood plug-in estimates in Equation (4), yielding $\hat{\Sigma}_Z = \Sigma_Z(\hat{\boldsymbol{\vartheta}}_{\text{ML}})$, $\hat{\Sigma}_{\text{PZ}} = \Sigma_{\text{PZ}}(\hat{\boldsymbol{\vartheta}}_{\text{ML}})$, and $\hat{\Sigma}_{\text{P}} = \Sigma_{\text{P}}(\hat{\boldsymbol{\vartheta}}_{\text{ML}})$.

For most applications, the assumptions of stationarity or isotropy are too restrictive, and more flexible covariance functions are needed to ensure the validity of (3) and (4). One popular approach to counter the lack of flexibility is the convolution approach introduced by Higdon et al. [1999], where the smooth process $Y(\cdot)$ is represented as the convolution of a white noise process $\varphi(\cdot)$, and a spatially-varying smoothing kernel $K(\cdot; \boldsymbol{\psi}_{\mathbf{s}})$ parameterized by a vector $\boldsymbol{\psi}_{\mathbf{s}}$ linked to the spatial location \mathbf{s} , by

$$Y(\mathbf{s}) = \int_{\mathcal{D}} K(\mathbf{u}; \boldsymbol{\psi}_{\mathbf{s}}) \varphi(\mathbf{u}) d\mathbf{u},$$

leading to the covariance kernel

$$\mathcal{C}(\mathbf{s}_i, \mathbf{s}_j; \boldsymbol{\psi}_{\mathbf{s}_i}, \boldsymbol{\psi}_{\mathbf{s}_j}) = \int_{\mathcal{D}} K(\mathbf{u}; \boldsymbol{\psi}_{\mathbf{s}_i}) K(\mathbf{u}; \boldsymbol{\psi}_{\mathbf{s}_j}) d\mathbf{u}. \quad (5)$$

Under this representation, it is straightforward to show that the covariance function is positive definite when employing valid kernels, i.e., kernels satisfying $\int_{\mathcal{R}^2} K(\mathbf{u}; \boldsymbol{\psi}_s) d\mathbf{u} < \infty$ and $\int_{\mathcal{R}^2} K^2(\mathbf{u}; \boldsymbol{\psi}_s) d\mathbf{u} < \infty$, evolving smoothly in \mathcal{D} . Defining valid kernels is considerably easier than defining positive-definite covariance functions, making the convolution approach more appealing when modeling nonstationary processes in the covariance. Paciorek and Schervish [2006] introduced a class of models based on (5) for which the integrations can be carried out analytically. They define the smoothing kernels $K_\ell = K(\cdot; \boldsymbol{\psi}_{\mathbf{s}_\ell})$ as multivariate Gaussian kernels centered at location \mathbf{s}_ℓ , leading to a covariance function with an integration-free form. The resulting covariance function can also be extended considering information about the smoothness of the process (introduced in Stein, 2005) as well as nonstationarity in the variance, leading to the nonstationary covariance function

$$\mathcal{C}_{NS}(\mathbf{s}_i, \mathbf{s}_j; \boldsymbol{\psi}_i, \boldsymbol{\psi}_j) = \sigma_i \sigma_j |\boldsymbol{\Sigma}_i|^{1/4} |\boldsymbol{\Sigma}_j|^{1/4} \left| \frac{\boldsymbol{\Sigma}_i + \boldsymbol{\Sigma}_j}{2} \right|^{-\frac{1}{2}} \mathcal{M}_{(\nu_i + \nu_j)/2}(\sqrt{Q_{ij}}), \quad (6)$$

where $\sigma_\ell = \sigma(\mathbf{s}_\ell)$ is a standard deviation process, $\nu_\ell = \nu(\mathbf{s}_\ell)$ is a smoothness process, $\mathcal{M}_\nu(\cdot)$ is the Matérn correlation function with smoothness ν and a deliberate valid scale parameter, $\boldsymbol{\Sigma}_\ell = \boldsymbol{\Sigma}(\boldsymbol{\psi}_\ell)$ is a 2×2 positive-definite covariance matrix process of the Gaussian kernel (i.e., the covariance kernel), and where $Q_{ij} = h_{(\boldsymbol{\Sigma}_i + \boldsymbol{\Sigma}_j)/2}$ is a semi-metric distance function [Schoenberg, 1938] defined as

$$Q_{ij} = (\mathbf{s}_i - \mathbf{s}_j)^\top \left(\frac{\boldsymbol{\Sigma}_i + \boldsymbol{\Sigma}_j}{2} \right)^{-1} (\mathbf{s}_i - \mathbf{s}_j), \quad \mathbf{s}_i, \mathbf{s}_j \in \mathcal{D}, \quad (7)$$

mimicking a geometrical anisotropic distance with an affine matrix defined by the average of the two covariance kernels at locations \mathbf{s}_i and \mathbf{s}_j . The resulting covariance function (6) is positive definite due to the validity of the kernels. This covariance function yields locally stationary spatial structures, which refer to ellipsoidal correlation profiles around a given spatial location \mathbf{s}_ℓ , decreasing with distance. The diagonal elements of $\boldsymbol{\Sigma}(\cdot)$ control how fast the correlation decays in one of the main axes defined by the locations, while the non-diagonal element controls the rotation of the principal axis of these ellipsoids.

Based on $\mathcal{C}_{NS}(\cdot, \cdot)$, Risser and Calder [2015] adopts parametric functions for the spatial standard deviation $\sigma(\cdot)$ and the local anisotropic structure $\boldsymbol{\Sigma}(\cdot)$, seeking a low-dimensional parametric space, stating a convenient compromise between the flexibility of $\mathcal{C}_{NS}(\cdot, \cdot)$ and computational requirements. They assume a linear model for the logarithm of the standard deviation, while for the covariance kernel they follow [Hoff and Niu, 2012] with the parametric model defined as

$$\boldsymbol{\Sigma}(\mathbf{s}_\ell) = \mathbf{A} + \mathbf{B} \mathbf{x}_\ell \mathbf{x}_\ell^\top \mathbf{B}^\top,$$

where \mathbf{A} is a $d \times d$ symmetric positive definite matrix representing an error covariance and where \mathbf{B} is a $d \times p$ matrix of rank 1 with coefficients describing how additional variability is distributed across the d dimensions. They comment that \mathbf{A} is identifiable and \mathbf{B} is identifiable up to a sign, given an appropriate range of covariate values [Hoff and Niu, 2012].

While these covariance functions are highly useful for representing non-stationary processes, they also have limitations. The nonparametric nature of $\mathcal{C}_{NS}(\cdot; \cdot)$ poses challenges during the estimation routine and can lead to computational difficulties, while the nonparametric nature increases the risk of overfitting. Moreover, considering a spatially-varying smoothness without imposing extra restrictions can be extremely difficult to estimate, and one would rather consider fixing the smoothness parameter as a practical compromise [Stein, 2005]. On the other hand, the implementation by Risser and Calder trades off the flexibility of (6) by using an efficient framework that leverages available covariate information to shape the nonstationary spatial structure. However, this approach does not fully exploit the modularity perspective since it shares parameters between the diagonal and non-diagonal elements of the covariance kernel, imposing specific behaviors on local spatial structures. Furthermore, although a spatially-varying parametric function for the smoothness process is introduced theoretically, the implementation later reverts to a global smoothness parameter.

Although the covariate-based covariance function framework achieves a reasonable degree of regularization, it is crucial to do so without imposing substantial restrictions on the source and extent of flexibility of different types of nonstationarity. One key source of nonstationarity is the smoothness parameter, which is key for optimal interpolation, but it is often assumed to be modeled as a global common smoothness parameter or even fixed. Allowing flexibility in the wrong source of nonstationarity could lead to a distortive representation of the spatial dependencies of the process [Fuglstad et al., 2015], and with it, numerical instabilities and ill-posed covariance matrices, challenging the convenience of nonstationary approaches.

3 Modular nonstationary covariance functions

This section introduces a class of covariance functions based on the covariate regression framework, designed to ease the limitations of previous implementations. We achieve this by defining a set of parametric spatially-varying functions

for various sources of nonstationarity represented by (6), employing a frequentist approach to benefit from readily available and efficient software implementations. We begin by presenting the model in Section 3.1, then we explore the interpretability of the model in Section 3.2 and the feasibility of model selection procedures, and discuss how this covariance function can be adapted to handle very large datasets in Section 3.4. We conclude this section in Section 3.5, where we introduce some challenges and strategies related to covariate-based covariance functions.

3.1 A class of dense nonstationary covariate-based covariance functions

To create an economical yet flexible class of nonstationary covariance functions, we assume first that the underlying smooth spatial structure $Y(\cdot)$ follows the class of covariance functions given in (6), but by considering parametric spatially-varying functions for $\sigma(\cdot)$, $\nu(\cdot)$, and $\Sigma(\cdot)$ instead as stochastics processes. These structures define the multivariate function $\Psi(\cdot)$ (likely nonparametric in nature), which is based on a set of fixed and observable covariates \mathbf{x}_ℓ^* at a given location \mathbf{s}_ℓ , yielding $\psi_\ell = (\sigma_\ell, \text{vech}(\Sigma_\ell), \nu_\ell)^\top$. In practice, we approximate $\Psi(\cdot)$ with $\tilde{\Psi}(\cdot; \phi)$ such that each of its structures relies on economical parameterizations, with parameters represented in ϕ , and by relying only on limited covariate information $\mathbf{x}_\ell \in \mathcal{R}^{p+1}$, where potentially $p \ll w$. We restrict $\tilde{\Psi}(\cdot; \phi)$ to smooth functions and with low computational complexity. The first constraint guarantees that the spatially-varying functions give the process's local properties, while the second promotes computational efficiency. We model each of the parametric structures of $\tilde{\Psi}$ separately, allowing us to model independently different sources of nonstationarity.

Among the considered sources of nonstationarity, the anisotropic structure Σ is one of the most challenging to model since in the spatial domain, $\Sigma(\cdot)$ yields positive definite, symmetric 2×2 matrices, with three unique elements, $[\Sigma]_{1,1}$, $[\Sigma]_{2,2}$, and $[\Sigma]_{1,2}$. The function we propose for $\Sigma(\cdot; \theta)$ shapes the size of the kernel in each axis, with a third component representing the tilt of the kernel, i.e. the angle with respect to the first eigenvector. We propose the following models for each of the elements of Σ

$$\Sigma(\cdot; \theta) = \rho(\cdot; \theta_{ms})^2 \begin{pmatrix} 1 & r(\cdot; \theta_{ga}) \cos(\omega(\cdot; \theta_{tt})) \\ r(\cdot; \theta_{ga})^2 & \end{pmatrix}, \quad (8)$$

where $\rho(\mathbf{x}_\ell; \theta_{ms}) = \exp(\mathbf{x}_\ell^\top \theta_{ms})$ governs the size of the kernel, controlled by a parameter vector θ_{ms} , $r(\mathbf{x}_\ell; \theta_{ga}) = \exp(\mathbf{x}_\ell^\top \theta_{ga})$ controls the shrink or expansion of the kernel in the secondary axis, controlled by a parameter vector θ_{ga} , and where $\cos(\omega(\mathbf{x}_\ell; \theta_{tt})) = \cos(\text{logit}^{-1}(\mathbf{x}_\ell^\top \theta_{tt})\pi)$ controls the correlation between the axes, controlled by a parameter vector θ_{tt} . We consider all the parameters handling the anisotropic structure in a vector $\theta = (\theta_{ms}^\top, \theta_{ga}^\top, \theta_{tt}^\top)^\top$. The subscripts ms , ga , and tt relate to main scale, geometric anisotropy, and tilt, i.e., sources of nonstationarity of the local geometric anisotropy $\Sigma(\cdot; \theta)$. Locally, $Q_{\ell\ell}$ takes the form of h_{Σ_ℓ} . This specific parameterization is similar to that derived from modeling the spherical coordinates of the Cholesky factor of Σ , rather than its raw elements [Pinheiro and Bates, 1996].

Continuing with the functions of $\tilde{\Psi}(\cdot; \phi)$, we have that $\text{Var}(Y(\mathbf{s}_\ell)) = \sigma^2(\mathbf{s}_\ell)$. We adopt the following model for the marginal standard deviation $\sigma(\cdot)$

$$\sigma(\mathbf{x}_\ell; \alpha) = \exp(0.5\mathbf{x}_\ell^\top \alpha),$$

where α is the associated parameter vector. However, the joint estimation of α and θ_{ms} will often lead to a set of highly correlated pairs of parameters associated to the same covariate (including the intercept), leading to an almost perfect correlation for very large sample sizes, as also mentioned in [Paciorek, 2003]. To ease this correlation while being able to recover the interpretability perspective, we consider instead the parameters $\alpha^{(d)}$ and $\theta_{ms}^{(d)}$ as $\alpha^{(d)} = \alpha + \theta_{ms}$, and $\theta_{ms}^{(d)} = \alpha - \theta_{ms}$, when a specific covariate X_ℓ is considered in both the standard deviation and the spatial scale functions.

Unlike the variance of a process, which is often estimated from data, the smoothness parameter is commonly fixed based on a priori knowledge of the process's inherent smoothness. This practice, part of the *geostatistical folklore* [De Oliveira and Han, 2022], often leads to inefficient spatial interpolation due to smoothness misspecification. This practice is primarily driven by theoretical considerations and numerical challenges. The former lies in the fact that the variance, scale, and smoothness parameters of the Matérn family cannot be consistently estimated for bounded domains under a single realization [Zhang, 2004], while numerical challenges arise due to estimating the smoothness parameter when considering expression outside of $\nu = i/2$, closed-form expression, due to the computationally expensive routines associated to $\mathcal{K}_\nu(\cdot)$ [Chen et al., 2024]. Extending the framework by considering spatially-varying smoothness without imposing some type of constraints can easily aggravate these challenges, making models with spatially-varying smoothness as in (6) extremely difficult to fit [Stein, 2005]. These challenges incentivize using a fixed global smoothness of the style $\nu = i/2$. Although modeling the smoothness based on covariates provides some degree of regularization, in practice, extra constraints must be made. Additional constraints can be imposed by restricting

the range of variability and by considering a numerically more stable approach when combining smoothness between locations. We implement the latter by, as opposed to modeling the spatially-varying smoothness as $\nu_{ij} = (\nu_i + \nu_j)/2$, representing it as $\nu_{ij} = \sqrt{\nu_i \nu_j}$, defining fundamentally different interweaving behaviors. While both representations behave similarly when $\nu_i \approx \nu_j$, $\sqrt{\nu_i \nu_j}$ yields a more conservative interweaving under highly discrepant smoothness. This leads to numerically more stable covariance matrices when compared to those based on $(\nu_i + \nu_j)/2$, allowing the representation of processes with highly heterogeneous smoothness at a local level, which are suitable, for example, for modeling strong discrepancies in the data, such as sharp jumps in the process. Moreover, to reduce the numerical challenges associated with the estimation of extreme values of smoothness, which are of little relevance in most applications, we model ν_i such that it restricts the range of variation, adding another layer of numerical stability. We constrain its variability within specified lower and upper bounds to better capture the inherent smoothness of the spatial process, leading to

$$\nu(\mathbf{x}_\ell; \zeta) = \frac{\nu_{\max} - \nu_{\min}}{1 + \exp(-\mathbf{x}_\ell^T \zeta)} + \nu_{\min}, \quad (9)$$

where ζ is the associated parametric vector, and where $0 < \nu_{\min} \leq \nu_{\max} < \infty$ refers to the lower and upper bounds of the smoothness. The proposed model (9) relates to a logistic cumulative density function with a fixed scale parameter, where we focus on shaping its location parameter.

This leads to the following general modular regression-based covariance function

$$\mathcal{C}_{GR}(\mathbf{s}_i, \mathbf{s}_j; \mathbf{x}_i, \mathbf{x}_j, \phi) = \sigma(\mathbf{x}_i; \alpha) \sigma(\mathbf{x}_j; \alpha) \frac{|\Sigma(\mathbf{x}_i; \theta)|^{1/4} |\Sigma(\mathbf{x}_j; \theta)|^{1/4}}{\left| \frac{\Sigma(\mathbf{x}_i; \theta) + \Sigma(\mathbf{x}_j; \theta)}{2} \right|^{1/2}} \mathcal{M}_{\nu(\mathbf{x}_i, \mathbf{x}_j; \xi)} \left(\sqrt{Q_{ij}} \right), \quad (10)$$

where $\phi = (\alpha^T, \theta_{ms}^T, \theta_{ga}^T, \theta_{tt}^T, \xi^T)^T$. In Appendix 6.1 we show that the resulting covariance function, particularly with the new parametric spatially-varying function for the smoothness, is positive definite.

3.2 Interpretability

The presented covariance model (10) provides a closed-form expression of the dependencies structure of the smooth process $Y(\cdot)$, by interweaving locally stationary geometrically anisotropic structures. In a small neighborhood around \mathbf{s}_ℓ , $\mathbf{s}_i \approx \mathbf{s}_\ell$, Equation (10) simplifies to

$$\mathcal{C}_{GR}(\mathbf{s}_i, \mathbf{s}_\ell; \mathbf{x}_\ell, \phi) \approx \sigma(\mathbf{x}_\ell; \alpha)^2 \mathcal{M}_{\nu(\mathbf{x}_\ell, \mathbf{x}_\ell; \xi)} \left(\sqrt{(\mathbf{s}_\ell - \mathbf{s}_i)^T \Sigma(\mathbf{x}_\ell; \theta)^{-1} (\mathbf{s}_\ell - \mathbf{s}_i)} \right), \quad (11)$$

defining stationary geometrically anisotropic Matérn covariance function with smoothness ν_ℓ . While ϕ unveils how a specific covariate influences a specific source of nonstationarity, inspecting the parametric structure at \mathbf{x}_ℓ characterizes its local dependency structure. The parameter ϕ of the nonstationary model (10) is identifiable, and parameters linked with covariates are centered, meaning that when $\theta_\ell = 0$, there is no effect of the covariate \mathbf{x}_ℓ over the specific spatially-varying function. Straightforward derivation of these relationships is that unit increases in \mathbf{x}_ℓ , holding other variables constant, results in the overall variance multiplying by $\exp(\alpha_{\cdot i})$, while for the smoothness parameters ξ , the inverse of the logit transformation of a parameter is associated with the local smoothness of the process.

Considering now the local anisotropy structure, the function Σ defines a 2×2 symmetric positive definite matrix, which relates to ellipsoids of a particular shape. Since we provide a model directly for the elements of Σ , it is not clear how the parameters of θ shape the associated kernel, for example, compared to a more classical representation of the kernel in spatial statistics as the spectral representation of Σ . To reveal this, we retrieve the associated eigenvalues and eigenvectors. The eigenvalues of the associated 2×2 symmetric positive definite matrix are defined by

$$e_{\ell, i} = \frac{\rho_\ell^2}{2} \left[(r_\ell^2 + 1) - (-1)^i \sqrt{(r_\ell^2 + 1)^2 - 4r_\ell^2 \sin(\omega_\ell)^2} \right], \quad i = 1, 2.$$

In general, the eigenvalues of Σ are well defined, except for the special case when $\omega = 0$ or $\omega = \pi$, where one of the eigenvalues collapses, though this is not a practical concern since these values are only achieved asymptotically. As special cases, the eigenvalues simplify to $(\rho_\ell^2, \rho_\ell^2 r_\ell)$ when $\omega_\ell = \pi/2$, and to $(\rho_\ell^2(1 + \cos(\omega_\ell)), \rho_\ell^2(1 - \cos(\omega_\ell)))$ when $r_\ell = 1$. Under these scenarios, both r and ω redistribute the trace of Σ along each eigenvalue, with the particularity that r_ℓ also influences the trace of Σ , while ω_ℓ does not.

To further inspect the representation of the ellipsoid based on Σ , we retrieve the associated eigenvectors. Each eigenvalue is associated with a specific eigenvector of the form

$$\mathbf{e}_{\ell, i} = \frac{s}{\sqrt{(2r_\ell \cos(\omega_\ell))^2 + (r_\ell^2 - 1 - (-1)^i A_\ell)^2}} \begin{pmatrix} 2r_\ell \cos(\omega_\ell) \\ r_\ell^2 - 1 - (-1)^i A_\ell \end{pmatrix}, \quad i = 1, 2,$$

where $A_\ell = \sqrt{(r_\ell^2 + 1)^2 - 4r_\ell^2 \sin(\omega_\ell)^2}$. The associated rotation angle given by the eigenvectors is $\arctan\left(\frac{r_\ell^2 - 1 + A_\ell}{2r \cos(\omega_\ell)}\right)$. In Figure 1 we present kernel ellipses defined by the eigenvalues with univariate changes with respect to r^2 in Panel (a), and ω in Panel (b). In Panel (c), we show the rotation angle (in radians) of the associate ellipsoid for different values of r^2 and ω , for values of $r^2 \leq 1$, and $\omega \leq \pi/2$. While the rotation angle is mainly driven for values of ω near $\pi/2$, the maximum rotation angle is restricted by r^2 , which mainly controls the rotation angle for low values of ω . Then, we can relate ω with the limited rotation of the ellipsoid. This behavior can be seen in more detail in Figure 2, where bivariate changes of ω and r^2 are presented. Under bivariate changes, expansion of the kernel in y -axis are given by $\sqrt{\rho r} \sin(\omega)$, and $\sqrt{\rho} \sin(\omega)$ in the x axis.

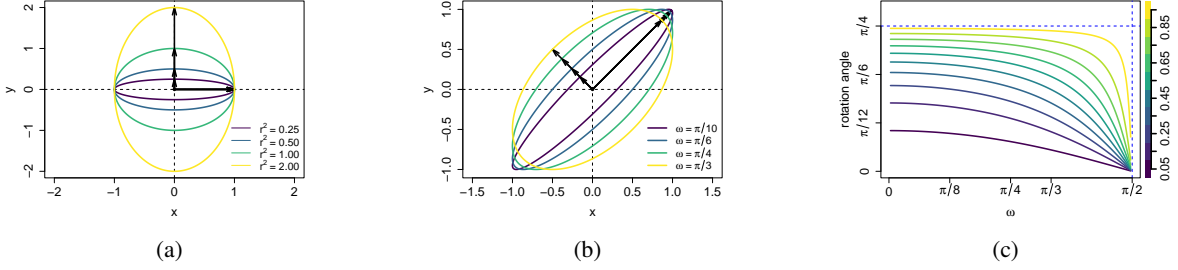


Figure 1: Kernel ellipses defined by the eigenvalues with univariate changes of r^2 (a) and ω (b), when $\omega = \pi/2$ and $r = 1$, respectively. In Panel (c) rotation angle (in radians) of the associate ellipsoid for different values of $r < 1$ (colored lines) and $\omega \leq \pi/2$.

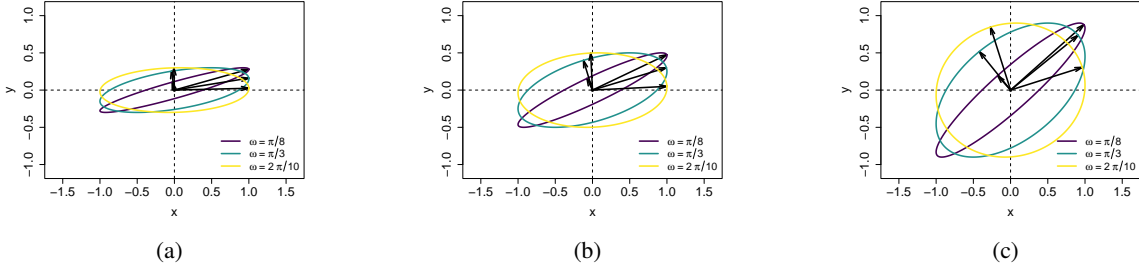


Figure 2: Ellipses defined by the eigenvalues for different values of ω and r . In Panel (a) $r^2 = 0.3$, Panel (b) $r^2 = 0.5$, and $r^2 = 0.9$ in Panel (c).

How the kernel Σ behaves is directly related to the representation of \sqrt{Q} locally. The proposed function for $\Sigma(\cdot; \theta)$ generalizes the common global types of anisotropic structures. In its simplest form, $\theta_{ga} = \theta_{tt} = 0$, and $\theta_{ms} = \theta_{ms}$, simplifies to a global isotropic scenario with a scale parameter equal to $\log(\theta_{ms})$. Global anisotropic structures can be retrieve when $\theta_{ga} \neq 0$ or when $\theta_{tt} \neq 0$. Considering $\theta_{tt} = 0$, and for locations \mathbf{s}_i and \mathbf{s}_j in a small neighborhood around a location \mathbf{s}_ℓ the scale for a given $\mathbf{s}_i - \mathbf{s}_j = (\Delta_x, \Delta_y)^T$ is then given by

$$\sqrt{Q_{ij}} = \frac{\sqrt{r_\ell^2 \Delta_x^2 + \Delta_y^2}}{\rho_\ell r_\ell},$$

where pure differences in the x -axis are related to a scale of ρ_ℓ , while pure differences in the y -axis have associated a scale that shrinks or expands by the parameter r_ℓ . r_ℓ takes the role of that associated with geometric anisotropy from classical geostatistics. Once we also consider $\theta_{tt} \neq 0$, the semi-distance metric takes the shape of

$$\sqrt{Q_{ij}} = \frac{\sqrt{r_\ell^2 \Delta_x^2 + \Delta_y^2 + 2\Delta_x \Delta_y r_\ell \cos(\alpha_\ell)}}{\rho_\ell r_\ell \sin(\alpha_\ell)},$$

where pure differences in the x -axis will lead to a scale given by $\rho_\ell \sin(\alpha_\ell)$. On the other hand, pure differences in the y -axis will lead to a scale given by $\rho_\ell r_\ell \sin(\alpha_\ell)$.

3.3 A simulation study exploring finite-sample confidence interval and likelihood ratio test

Alongside the MLE of ϕ , confidence intervals are often of interest. These intervals, such as univariate Wald confidence intervals, require a measurement of the standard error of $\hat{\phi}_{ML}$, which is typically approximated by relying on the

asymptotic properties of the MLE for a given framework. However, little is known about the limiting distribution of the MLE with nonstationary covariance models under any of the available asymptotic frameworks in spatial statistics. Moreover, it is often interesting to compare nested models, for which the likelihood ratio test can be useful, though there is no certainty about the distributional assumption of the likelihood ratio test between models that differ mainly over covariance structures. To investigate this, we run a small simulation study in which we assess the finite-sample confidence intervals and the feasibility of the likelihood ratio test when comparing models that differ in their covariance models.

In particular, we assess the feasibility of the asymptotic distribution for MLE's provided by Mardia and Marshall [1984], which shows that under certain regularity conditions, the MLE of $\boldsymbol{\theta}$ is consistent and asymptotically Gaussian, with an asymptotic covariance matrix equal to the inverse of the Fisher information matrix. Furthermore, we are particularly interested in deriving confidence intervals for functions of the MLE's, such as for the global variance parameter $\gamma(\boldsymbol{\phi}) = \frac{\alpha_1^{(d)} + \theta_{mr,1}^{(d)}}{2}$, leading to

$$\hat{\gamma} \stackrel{approx}{\sim} \mathcal{N}(\gamma, \nabla\gamma(\hat{\boldsymbol{\phi}})^T \mathbf{I}(\hat{\boldsymbol{\phi}})^{-1} \nabla\gamma(\hat{\boldsymbol{\phi}})), \quad (12)$$

where $\mathbf{I}(\hat{\boldsymbol{\phi}})^{-1}$ is the 2×2 matrix with the approximate inverse of the Fisher information matrix related to the parameters $\alpha_1^{(d)}$, $\theta_{mr,1}^{(d)}$, and where $\nabla\gamma(\boldsymbol{\phi})$ is the gradient vector of $\gamma(\boldsymbol{\phi})$. Given the lack of analytic expression for the Fisher information matrix, we instead assess it with the numerically approximated Hessian.

The simulation study consists of two parts. First, we evaluate the coverage probability of Wald type confidence interval for a set of nominal significance levels of 0.01, 0.05, and 0.10. We sample 1000 realizations of a centered Gaussian process with nonstationary covariance model as in (10), in $\mathcal{D} \in [-0.5, 0.5]^2$ for different sample sizes $n = 100, 200, 400, 800$. Notice that the considered sequence of sample sizes does not align with the asymptotic framework presented by Mardia, but it is arguably more relevant in the spatial context. The covariance model considers a global standard deviation $\alpha_1 = 0$ and scale $\theta_{mr,1} = \log(0.25)$, and a fixed known smoothness parameter $\nu = 1.5$. We also consider a spatially-varying standard deviation and scale of $\alpha_2 = 0.5$ and $\theta_{mr,2} = -0.25$, linked to a sinusoidal covariate that evolves across the x -axis defined by $\sin(10x)$. Then $\sigma(\mathbf{s}_\ell; \boldsymbol{\alpha}) = \exp(0.5(\alpha_1 + \alpha_2 x_\ell))$ and $\rho(\mathbf{s}_\ell; \boldsymbol{\theta}_{ms}) = \exp(\theta_{ms,1} + \theta_{ms,2} \mathbf{x}_\ell)$. At every iteration, we construct the univariate Wald-type confidence intervals, with standard errors derived from the inverse of the approximated Hessian.

In the second part, we assess the performance of the log-likelihood ratio test when comparing models considering spatially-varying scale and variance, and another with spatially-varying scale, with a stationary isotropic Gaussian process in $\mathcal{D} \in [-0.5, 0.5]^2$, when the latter is the true underlying model. We estimate type I errors and compare them to the nominal values of 0.01, 0.05, and 0.10. We shape both source of nonstationarity based on the same sinusoidal covariate across the x -axis.

Table 1 presents the results for the first part of the simulation study. We also report the empirical bias for each parameter at different sample sizes. Although the increase in sample size does not seem to considerably improve the empirical coverage probabilities, there is an overall agreement between them. The empirical coverage probabilities are lower than the nominal values, with slightly worse performance for the scenario of 0.1, which, considering the nonexistent bias, suggests that the approximated standard errors are smaller than they should be, likely due to the behavior of the ML estimator under bounded spatial frameworks (Gelfand et al. [2010]).

Table 1: Empirical coverage probabilities of univariate Wald-type confidence intervals for different nominal values and sample sizes. The first column of each block presents the empirical mean across the 1000 iterations for the respective parameter.

n	α_2				$\theta_{ms,2}$			
	mean($\hat{\alpha}_2$)	0.99	0.95	0.90	mean($\hat{\theta}_{ms,2}$)	0.99	0.95	0.90
100	0.504	0.975	0.935	0.879	-0.255	0.967	0.922	0.874
200	0.508	0.986	0.931	0.876	-0.250	0.981	0.928	0.873
400	0.510	0.984	0.927	0.887	-0.246	0.979	0.930	0.885
800	0.505	0.980	0.940	0.879	-0.249	0.984	0.931	0.888

In Table 2 we present the results of the simulation study for the likelihood ratio test. We also report the Kolmogorov-Smirnov statistic obtained by the 1000 simulations for each sample size scenario, defined as

$$D_n = \sup_x |\mathcal{F}_n(x) - \mathcal{F}(x)|, \quad (13)$$

where $\mathcal{F}_n(\cdot)$ is the empirical distribution function defined as $\mathcal{F}_n(x) = 1/n \sum_{i=1}^n I_{(-\infty, x]}(y_i)$, where $I_{(-\infty, x]}(y_i)$ is an indicator function equal to 1 when $y_i \leq x$, and where $\mathcal{F}(\cdot)$ follows a χ^2 cumulative density function with one or

two degree of freedoms, depending on the sampling scenario. Overall, there is a good agreement for $q = 1$ between the empirical type I probabilities and nominal ones, where increasing the sample size does not seem to improve the empirical type I probabilities. The low values of D_n indicate little discrepancy between the empirical and theoretical distribution. An exception seems to be when $q = 2$, since an increase in sample size leads to an increase of the type I probability error, supported by the (slight) increase in the test statistic D_n . An inflated type I error suggests that the model is overfitting by explaining random noise with a spatially-varying marginal standard and scale.

Table 2: Empirical Type I errors for different nominal levels and sample sizes. The last two columns present the Kolmogorov-Smirnov statistics for different scenarios and sample sizes.

n	$q = 1$			$q = 2$			D_n	
	0.01	0.05	0.1	0.01	0.05	0.1	$q = 1$	$q = 2$
100	0.008	0.059	0.102	0.011	0.054	0.108	0.03	0.02
200	0.013	0.045	0.099	0.022	0.060	0.105	0.02	0.03
400	0.013	0.064	0.122	0.017	0.076	0.136	0.03	0.05
800	0.010	0.057	0.107	0.019	0.080	0.150	0.02	0.06

Based on the results from the simulation studies, both confidence intervals and likelihood ratio test can aid in model selection, favoring less complex models unless there is substantial evidence that they fit poorly. Model selection in spatial statistics is particularly challenging due to the computationally expensive routines associated with the MLE's even under moderate sample sizes, which limits approaches such as (informally) comparing the Akaike Information Criterion (AIC) [Akaike, 1998] or the Bayesian information criterion (BIC) between a pool of competing models, or by (formally) testing through a likelihood ratio test nested models. The feasibility of the likelihood ratio test, in combination with the parametric and modular structure of (10), provides a framework to test for specific sources of nonstationary and to compare nested models, such as the scenario analyzed in the likelihood ratio test simulation study, where we were assessing whether a nonstationary covariance function in the scale and variance explained the data using a Matérn model. On the other hand, confidence intervals from a "full" model might be a good starting point for narrowing the number of competing models to compare them through AIC or BIC.

3.4 A class of sparse covariate-based covariance functions

Employing dense covariance matrices such as (10) can be challenging for large sample sizes, mainly due to the evaluation of $\det(\Sigma_Z)$ and solving linear systems involving Σ_Z , requiring $O(n^3)$ floating point operations and $O(n^2)$ memory. A well-known workaround for computational challenges in spatial prediction is the Tapering Approach (TA) [Furrer et al., 2006], which aims to induce sparsity into the covariance matrix to benefit from fast and accurate algorithms tailored to sparse matrices. This sparsity is achieved by multiplying element-wise the covariance matrix Σ_Z with a valid compact-supported correlation matrix, known as the taper matrix.

Considering \mathbf{T}_δ as the $n \times n$ positive-definite taper matrix based on a compact-supported correlation function with scale parameter δ , the tapered matrix is then defined as

$$\Sigma_T = \Sigma_Z \odot \mathbf{T}_\delta, \quad (14)$$

where \odot denotes the Schur or element-wise product, and δ controls the number of induced zeroes in the tapered matrix. When $\delta \rightarrow 0$, Σ_T simplifies to a diagonal matrix, and when $\delta \rightarrow \infty$, recovers Σ_Z . In practice, the degree of induced sparsity can be considerably large, often leading to a covariance matrix of only 1% of non-zero elements. As a rule of thumb, considering between 50 to 100 observations should be sufficient for predictions under a Matérn model [Blasi et al., 2022].

The presented covariance model (6) can easily and efficiently be adapted for TA. We propose a simplification of the nonstationary model (10) by considering spatially-varying local structures concerning scale, smoothness, and variance, leading to

$$\mathcal{C}_s(\mathbf{s}_i, \mathbf{s}_j; \mathbf{x}_i, \mathbf{x}_j, \phi) = \sigma_i \sigma_j 2^{\frac{1/2 \rho_i}{\rho_i} \frac{1/2 \rho_j}{\rho_j}} \mathcal{M}_{\nu_{ij}^*} \left(\sqrt{\frac{h}{\frac{\rho_i + \rho_j}{2}}} \right), \quad (15)$$

where Q_{ij} has simplified to $h / \frac{\rho_i + \rho_j}{2}$, which entails a local stationary structure at location \mathbf{s}_ℓ with a scale parameter ρ_ℓ . Given that this is a special case to the family of covariance functions presented in 3, it is still positive definite. The considered sources of nonstationarity yields a set of local stationary isotropic spatial structures that differ in smoothness, variance, and local isotropic structures with different scales. The proposed model for the spatially-varying smoothness present two advantages under this framework. Firstly, under very large sample sizes, it is convenient to control the extent of variability of the spatially-varying smoothness, which can cause numerical instabilities. Secondly, under TA, it

is common practice to select a common taper function that is at least as smooth as the dense covariance function, which can be achieved by the ν_{\max} hyperparameter. In Appendix 6.4, we present some of the most popular compact-supported correlation functions, such as the Spherical and Wendland covariance models [Bevilacqua et al., 2019].

Estimation of ϑ is done by maximizing

$$l_{\mathbf{T}}(\vartheta) = -\frac{n}{2} \log(2\pi) - \frac{1}{2} \log \det(\Sigma_{\mathbf{Z}} \odot \mathbf{T}_{\delta}) - \frac{1}{2} (\mathbf{z} - \mathbf{X}\boldsymbol{\beta})^{\mathbf{T}} (\Sigma_{\mathbf{Z}} \odot \mathbf{T}_{\delta})^{-1} (\mathbf{z} - \mathbf{X}\boldsymbol{\beta}). \quad (16)$$

In practice, there is a tradeoff between the taper scale δ and the bias of the estimates, especially if δ is small relative to the true correlation scale of the process.

3.5 Challenges of covariate-based covariance functions

The covariate-based covariance regression approach offers a good balance between flexibility and computational efficiency while adding a layer of interpretability. However, it does come with some challenges. Certain types of covariates may distort the local properties of the spatial structure, and in some situations, regularization will be required, as is common to nonstationary covariance functions in a maximum likelihood framework.

A key assumption of convolution-based covariate functions is that the kernels evolve smoothly over the study domain \mathcal{D} . Then, the local properties of the spatial structure of the process are well represented by the functional form of the proposed covariance function. This assumption is sensible to the functional form of $\tilde{\Psi}(\cdot; \phi)$ and consequently depends on the nature of the covariates used. This naturally raises questions about the types of covariates suitable for modeling $\tilde{\Psi}(\cdot; \phi)$. Ordinal variables and noisy covariates will not meet this assumption and will impose spurious behaviors. Given that these types of covariates are frequently used when modeling spatial data, we comment on the consequences of employing these type of covariates over the covariance function.

When considering ordinal variables, while the local stationarity assumption holds within the same level, covariance between levels can exhibit a reduced correlation regardless of the spatial scale. In Panel (a) and Panel (b) of Figure 3 we present an example for a realization of a process in \mathcal{R}^1 . In \mathcal{R}^1 , the anisotropic structure simplifies to $\Sigma(\cdot) = \rho(\cdot)$, a varying scale function in \mathcal{R}^1 . Although the local stationarity assumption holds for values of the categorical variable of the same level, there is a break between levels. The reduction of correlation between levels is caused by the prefactor, i.e., the ratio of determinants in (6), regardless of how close and strong the spatial scale is at both levels. For example, a local scale of 1 and 10 at each level would lead to a prefactor of approximately 0.6, meaning that irrespective of how close the locations between levels are, the maximum correlation will be 0.6. This is generally undesirable in most scenarios and can impact the model's performance.

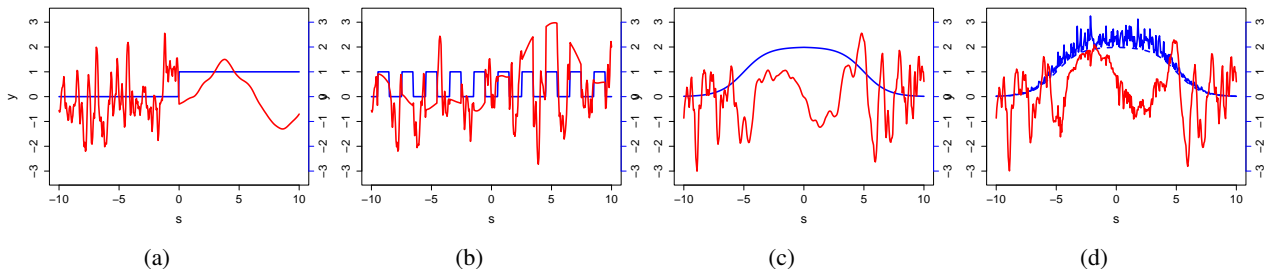


Figure 3: In red, four realizations of stationary Gaussian processes in \mathcal{R}^1 . In the first two Panels, the spatially-varying scale with an ordinal variable is modeled (with one jump and several jumps). The last two Panels, with a smooth and noisy covariate, respectively. In blue is the covariate information. All process realizations were simulated with the same seed.

The same challenges are also present when employing noisy covariates. In particular, when noisy covariates are considered in the covariance kernel $\Sigma(\cdot; \theta)$ and the smoothness $\nu(\cdot, \cdot; \xi)$. The former goes align as when employing categorical variables, inducing an overall reduction of the correlation due to the prefactor, while employing noisy covariates in the smoothness can trigger numerical challenges due to the discrepancy of local behaviors, impacting the first off-diagonal elements of the covariance matrix. In Figure 3 we exemplify these behaviors in \mathcal{R}^1 . We see that although in Panel (d), the associate scale should increase given that the noisy version is at least the value of the smooth covariate (implying a strongly correlated process), the inherent noise of the covariate leads to a process exhibiting a combination of a higher correlation with jittering.

The last challenge addressed in this section concerns the numerical challenges that often arise when dealing with nonstationary covariance functions. Regularization is often needed to prevent that the associated covariance matrix is

ill-posed, whether due to weakly identifiable parameters, a densely sampled domain, or an inherently challenging spatial structure. One simple regularization approach is to consider $\sigma_\varepsilon^2 > 0$, typically ranging from $1e - 8$ up to $1e - 1$ of the global variance, promoting numerical stability [Basak et al., 2021]. However, this yields discontinuities at the origin of the covariance function, which can affect the estimability of the smoothness and scale parameters of the Matérn covariance function [Andrianakis and Challenor, 2012].

Given the modular structure of the presented covariance function, we instead propose a simple yet efficient regularization approach based on a penalized maximum likelihood framework, where we promote numerical stability by penalizing the product $\sqrt{\nu_0}\rho_0$, being ν_0 and ρ_0 the smoothness and spatial scale when all $\mathbf{x}_\ell = 0, \ell > 1$. This leads to a penalized maximum likelihood function defined as

$$l_{pen}(\boldsymbol{\vartheta}) = l(\boldsymbol{\vartheta}) + n\lambda\sqrt{\nu_0}\rho_0, \quad (17)$$

where $\lambda \geq 0$ is the penalization parameter, and where $\hat{\boldsymbol{\vartheta}}_{pen}$ is the vector resulting of maximizing $l_{pen}(\cdot)$. By penalizing the product $\sqrt{\nu_0}\rho_0$, we are discouraging highly-smoothed, long-tailed covariance functions, which are the most challenging types of covariance functions to represent at a numerical level. No penalization is present when $\lambda = 0$, and $l_{pen}(\cdot)$ falls back to the traditional log-likelihood function. On the other hand, as $\lambda \rightarrow \infty, \rho \rightarrow 0$ and $\nu \rightarrow \nu_{min}$, incentivizing less complex models. While predictions based on models with a fixed nugget effect are approximators, i.e., prediction at location \mathbf{s}_ℓ based on (4) is not equal to the observed response $z(\mathbf{s}_\ell)$, predictions based on $\hat{\boldsymbol{\vartheta}}_{pen}$ preserves the property of interpolating at observed locations \mathbf{s}_ℓ , which might be more convenient under deterministic simulation applications [Peng and Wu, 2014].

The presented penalized approach induces bias in the estimates, promoting short-tailed covariance functions, and with it, an improvement of the associated covariance matrix's numerical stability. We exemplify this trade-off in Figure 4, where we model a nonstationary Gaussian process in the spatial trend, variance, and scale, shaped with sinusoidal covariates in each axis. As the regularization parameter increases, the numerical stability of the covariance matrix based on $\hat{\boldsymbol{\vartheta}}_{pen}$ improves as shown in Panel (a), represented through the condition number of the associated covariance matrix, with smaller values indicating better numerical behavior. This reduction of the condition number is mainly achieved due to the reduction of $\boldsymbol{\vartheta}_{ms,1}$ as shown in Panel (b), reducing the overall extent of the local covariance structures. Alongside this reduction, α_1 also decreases, while ξ_1 (although penalized) increases to compensate for the constrained representations of the covariance function. This behavior of \mathbf{x}_1 compensating the reduction of $\boldsymbol{\vartheta}_{ms,1}$ will change for large penalization values, where both parameters tend to decrease together. These changes seem only slightly affect β_0 and those parameters associated with spatially-varying sources of nonstationarity. Although there are sizable changes in the estimates for large penalization values, it will often have only a minor impact on prediction capabilities. In Panel (c), we highlight how the Root Mean Square Prediction Error (RMSPE) as well as the Continuous Rank Probability Score (CRPS) (which is formally introduced in Section 4.3) relative to the scenario with no penalization remains within 3%. The CRPS, which does not only account for point accuracy but also for adequate uncertainty quantification, as well as the RMSPE, provide better prediction capabilities for small regularization parameters. This slight improvement is likely due to the tendency of the model to overfit when considering both spatially-varying variance and scale, as observed in 3.3.

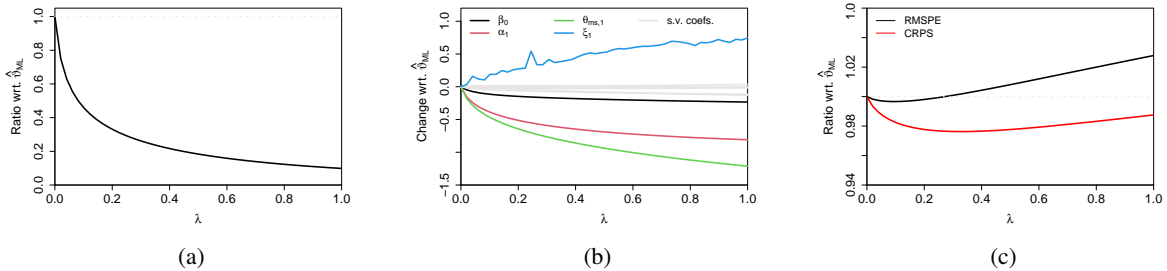


Figure 4: Summary metrics under different penalization values. The condition number is presented in Panel (a), relative change of $\hat{\boldsymbol{\vartheta}}_{pen}$ in Panel (b), and prediction metrics in Panel (c).

4 Illustration

In this section, we fit Gaussian processes to monthly precipitation data with covariance functions presented in 3.1 and 3.4 to inspect the type and nature of nonstationarity of the data. Then, we assess their predictive performance based on held-out data, compared to classical implementations, and with alternative models to evaluate the effect on prediction

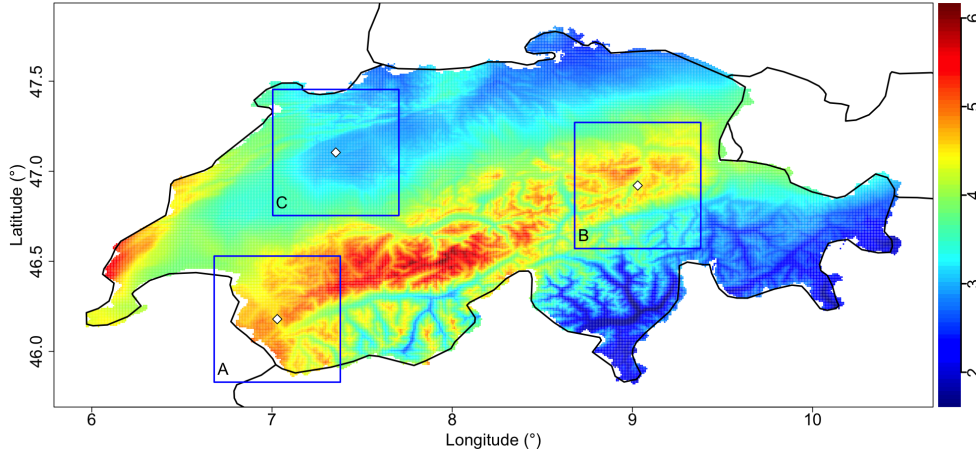


Figure 5: Average daily precipitation measured in millimeters for the month of January for the period 1979-2018 derived from ERA5. Regions within blue rectangles with respect to white diamonds at each center are inspected with a closer look.

skills by considering a spatially-varying smoothness. The implementations rely heavily on the `cocons` R package [Blasi, 2024], which provides most of the typical statistical procedures to model and predict Gaussian processes with the presented class of covariance functions.

4.1 Data

We use data from the Copernicus Europe repository, which offers a wide range of down-scaled bioclimatic indicators at a 1×1 km resolution, derived from ERA5 and ERA5-Land reanalysis of a 12-year period (1979-2018) [Wouters, 2021]. Such datasets are extensively used in the biodiversity community for climate screening analyses and various downstream applications. We focus on locations within Switzerland, contained within latitudes $45^{\circ}75'$ to $47^{\circ}93'$ and longitudes 6° to $10^{\circ}69'$. We model the daily average precipitation for January for the period 1979-2018, shaping the nonstationarity in the spatial trend and covariance with bioclimatic indicators. Additionally, we consider latitude and longitude, and we collect elevation data using the R package `elevatr` [Hollister et al., 2021]. Instructions for accessing, downloading, and preprocessing the data are presented in Appendix 6.5.

Table 3: Description of covariates

Label	Variable	Description
prec	Precipitation	January daily average precipitation over the entire time period (mm)
wind	Wind	January daily average magnitude over the entire time period of the two-dimensional horizontal air velocity near the surface over the entire time period (ms^{-1})
merwind	Meridional wind speed	January daily average magnitude over the entire time period of the northward component of the two-dimensional horizontal air velocity near the surface (ms^{-1})
elev	Elevation	Elevation (mts)
BI004	Temperature seasonality	Standard deviation of the monthly mean temperature multiplied by 100 (K)
BI015	Precipitation seasonality	Annual coefficient of variation of the monthly precipitation (-)
cloud	Cloud coverage	January daily average over the entire time period of the fraction of the grid for which the sky is covered with clouds. Clouds at any height above the surface are considered (as a fraction)

In Table 3, Figure 5, and Figure 6 we present an overview of the covariates. Switzerland is characterized by its geographically diverse terrain, encompassing a mixture of wide, flat, low-altitude regions in the North with mountainous regions in the center and South, including the Alps and Jura Mountains, with narrow valleys dissecting these areas. When accounting for bioclimatic aspects such as cloud cover and wind patterns, distinct spatial structures with highly heterogeneous characteristics emerge. These factors greatly influence the spatial distribution of precipitation fields, requiring more flexible models.

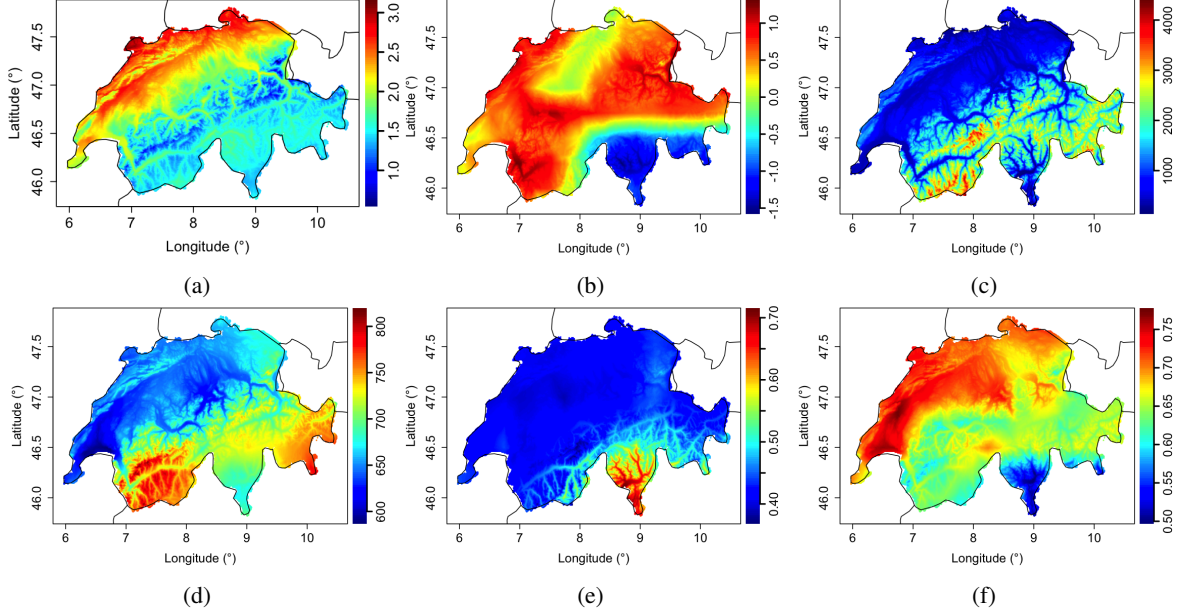


Figure 6: Down-scaled bioclimatic indicators: wind (a), meridional wind speed (b), elevation (c), temperature seasonality (d), precipitation seasonality (e), and cloud coverage (f). The heterogeneous covariates across Switzerland promote nonstationarity in both spatial trend and spatial structure.

4.2 Framework

To address the different frameworks for which the presented covariance functions are tailored, we consider two distinct scenarios: one with dense covariance functions ($n = 500$) and another with sparse covariance functions ($n = 10000$). Additionally, we use a hold-out dataset comprising 18781 prediction locations based on a mix of random samples, stripes of varying widths, and small clusters to thoroughly evaluate the performance of the covariance functions across diverse spatial configurations.

Given the difficulty of exploring nonstationary spatial structures a priori, we first fit *full* models considering cloud coverage, elevation, wind, latitude, and longitude covariates in all the different sources of nonstationarity of the spatial structure, introduced as logarithms to linearize their effects, which are then scaled to improve numerical stability. For the spatial trend component, we use a common trend for all models in both frameworks, involving scaled versions of all presented covariates in Figure 6 plus latitude and longitude. A reduced version (M-NS) was identified based on the full model, yielding a lower BIC and preserving all spatially-varying functions. The BIC comparison was made informally, given that a regularization was needed ($\lambda = 0.025\sqrt{8}$). To facilitate comparison, we consider two additional models. The first, based on M-NS, simplifies the spatially-varying smoothness to a global parameter (M-GS). The second is a classical Matérn model with $\lambda = 0$ and a global anisotropic structure (M-STAT). For all three models, we set $\nu_{\min} = 0.5$ and $\nu_{\max} = 2.0$. A table summarizing the model structures is provided in Appendix 6.3.

We consider a similar set of models for the sparse scenario. The first model employs a spatially-varying variance, scale, and smoothness (M-NS-T) with a regularization parameter $\lambda = 0.0125\sqrt{8}$. The second model, M-GS-T, simplifies the spatially-varying smoothness to a single global parameter, while the third model is a classical Tapered Matérn covariance function (M-STAT-T). We select Wendland₁ and Wendland₂ taper functions for the stationary and nonstationary models, respectively, with a common taper scale of $\rho = 0.23$, resulting in slightly above 3% non-zero elements. For M-STAT-T we use $\nu_{\min} = 0.25$ and $\nu_{\max} = 1.5$, and for the taper-based nonstationary models, we set $\nu_{\min} = 0.5$ and $\nu_{\max} = 2.5$. Given the computational cost of estimating Taper-based models, we estimate M-NS-T and M-GS-T based on all covariates, and therefore, no (informal) model selection was done.

4.3 Evaluation criteria

To assess the performance of the models on the held-out dataset, we consider several criteria, including the Continuous Rank Probability Score (CRPS) and Log-Score [Gneiting and Raftery, 2007], Root Mean Square Prediction Error

(RMSPE), the Kolmogorov-Smirnov test statistics with respect to a standardized Gaussian distribution (D_n), as well as the empirical coverage probability of prediction intervals for a nominal level of 0.05 (CPI).

We also report the number of parameters of the model, penalized log-likelihood values, and the computational time required to run the numerical optimizer L-BFGS-B. Instead of evaluating these criteria on the full hold-out sample, we split it into 100 different sets of hold-out samples defined by a k-means algorithm creating heterogeneous scenarios to assess prediction capabilities of the models over a wide range of scenarios and spatial locations with heterogeneous characteristics. By calculating these criteria for each set, we account for the variability in prediction accuracy due to the selection of specific hold-out samples.

While RMSPE summarizes model quality in terms of bias, both the CRPS and Log-Rank incorporate information about the uncertainty of the prediction distribution, making it more informative for comparing models with different spatial structures. The *best* score is achieved when the held-out data align perfectly with their predictive distributions [Gneiting and Raftery, 2007]. For Gaussian processes, the CRPS at prediction location \mathbf{s}_ℓ^p is defined as

$$\text{CRPS}(\mathbf{s}_\ell^p) = \sigma_\ell \left[\frac{1}{\sqrt{\pi}} - 2\mathcal{N}_{\text{pdf}}\left(\frac{z_\ell^p - \mu_\ell}{\sigma_\ell}\right) - \left(\frac{z_\ell^p - \mu_\ell}{\sigma_\ell}\right) \left(2\mathcal{N}_{\text{cdf}}\left(\frac{z_\ell^p - \mu_\ell}{\sigma_\ell}\right) - 1\right) \right], \quad (18)$$

where μ_ℓ and σ_ℓ are the mean and standard deviation at prediction location \mathbf{s}_ℓ^p , and where \mathcal{N}_{pdf} and \mathcal{N}_{cdf} are the standardized univariate Gaussian density and cumulative functions, respectively. The Log-Score, on the other hand, takes the form of

$$\text{Log-Score}(\mathbf{s}_\ell^p) = \log(\sqrt{2\pi}) + \left(\frac{z_\ell^p - \mu_\ell}{\sqrt{2}\sigma_\ell}\right)^2 + \log(\sigma_\ell). \quad (19)$$

We estimate the CRPS and the Log-Score using plug-in estimates for the mean and variance of the predictive distribution. We report the mean across holdouts for the CRPS, its empirical 0.95 quantile, the Log-Score, D_n , and CPI.

4.4 Results

Prior to the spatial trend specification in 4.2, we initially considered a trend model with covariates such as latitude, longitude, wind, elevation, and cloud coverage. The marginal standard deviation and (approximate) local effective scale spatial surfaces are shown in Panel (a) and Panel (b) of Figure 7. The resulting spatial surfaces do not match our initial guess of these source of nonstationarity behaviors, localizing large marginal standard deviations and (approximate) local effective scale in the southern part of Switzerland, unveiling a strong component of latitude. The marginal standard deviation reaches up to five times the empirical standard deviation, while a large proportion of the local effective scale exceeds the maximum distance within the domain. The nonstationary model allows the trend to ease the fit over this region (as seen in Panel (c), where larger residuals are concentrated in the South region) by capturing these large residuals through an increase of the spatially-varying anisotropic structure and marginal standard deviation. Rather than tell us something about the physical behavior of the daily mean precipitation, this suggests a misspecification in the trend, resolved by an unrealistic spatial structure. Based on this knowledge, we improved the trend structure by extending it by adding temperature and precipitation seasonality, as well as meridional wind speed.

A comparison of the nonstationary model with the new trend structure (M-NS) is shown in Panel (d) and Panel (e) of Figure 7, whereas a summary of parameter estimates is shown in Appendix 6.3. The penalized log-likelihood decreased over 200 points compared to the initial model, indicating a considerable improvement by adding three more covariates to the trend. Both sources of nonstationarity now seems to vary more freely across the domain, with the spatial surface of the local effective scale capturing a large cluster of larger positive and negative residuals in the east and southern regions as seen in Panel (f), and whereas the marginal standard deviation is sensibly adjusting this region. The spatial surfaces of M-NS-T follow a similar pattern for the marginal standard deviations (besides the strong bias typically exhibited by the Taper-based models), but a highly contrasted behavior in Panel (h), where now low values of the (approximate) local effective scale are exhibited mostly over the mountainous region, opposite as for M-NS.

In Figure 8, we inspect how the correlation structure behaves for M-NS and M-NS-T at three distinct regions. Each column relates to the different boxes in Figure 5. The added flexibility of both models allows the spatial structure to adjust locally to the characteristics of the spatial locations, but without forcing nonstationary structures where it is not required. The correlation structure in Panel (a) with respect to the location at the white mark reduces drastically to the East-West due to the steep increase in elevation while keeping a high correlation within the valley locations aligned in the North-South direction, showing a stark contrast with how the fixed anisotropic structure in M-STAT prioritizes higher correlations. On the other hand, in Panels (b) and (c), the correlation structures with respect to the locations at the white marks are in higher agreement with those provided by M-STAT, with smoother adjustments, and almost perfect agreement in Panel (c), where the surrounding spatial characteristics do not induce strong modification of a simple, global anisotropic spatial structure. The same pattern holds for M-NS-T and its stationary counterpart, as shown in the

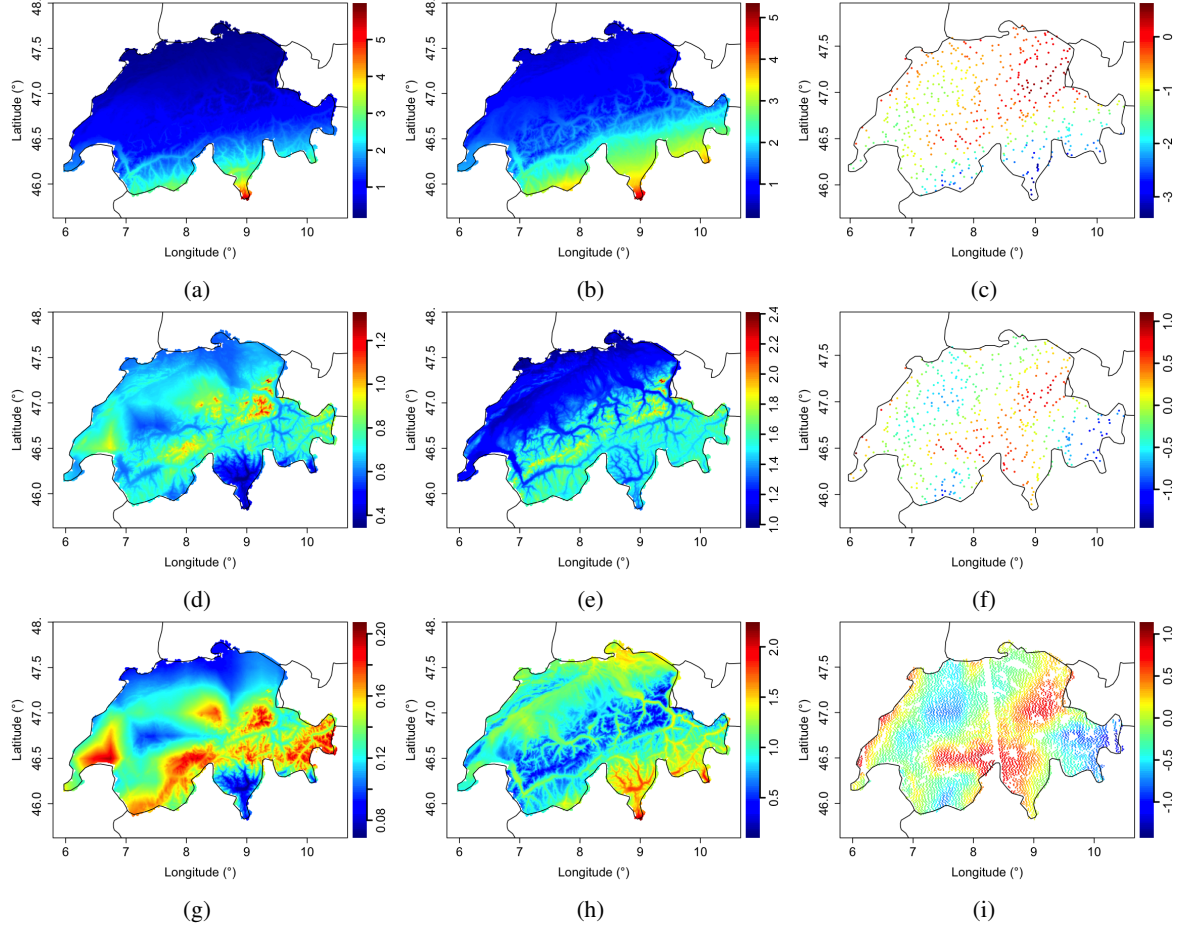


Figure 7: First two columns are the spatial surfaces over the full dataset of the marginal standard deviation and (approximate) local effective scale for different models. Third column presents residuals of different models over the training dataset. The first row relates to a misspecified model in the trend. The second row is from M-NS, while the third row relates to M-NS-T.

second row of Figure 8. Here, the correlation structure is restricted by the fixed taper scale, inducing the correlation to go to zero as Q_{ij} approaches $\delta = 0.23$. Still, we can see that the same intensity of adjustment is preserved across columns.

Although the trend surfaces of M-NS and M-STAT look similar at first glance, they show considerable differences when examined closely, limiting a direct comparison between the estimated parameters of their covariance functions. However, this does not change the central location of the estimated spatial surfaces compared to the global parameters of M-STAT. Some of the medians of the estimated spatial surfaces of the different source of nonstationarity are similar, i.e., the median of the spatially-varying scale is just 4% smaller (4.81 vs. 5.02), and the restricted tilt is mainly concentrated around zero, consistent with M-STAT. However, the median of the marginal standard deviation of M-NS is 27% larger than that of M-STAT (0.70 vs. 0.55).

While the strength of the discrepancies seems proportional to the flexibility of each spatially-varying function, this is not the case for the smoothness. M-NS-G, which has the same covariance function as M-NS but considers a global smoothness parameter, exhibits a smoothness parameter similar to the median of M-NS (1.54 vs. 1.61). Lower smoothness values, as in M-STAT, seem to be a way to account for inadequacies in model fit, as highlighted in [Paciorek, 2003]. Figure 9 shows the estimated spatial surfaces for the smoothness of both nonstationary models. There is a rather opposite behavior between the two spatial surfaces. As the resolution increases, it prioritizes larger smoothness over the wind (negatively) and elevation (positively) covariates, while for low sample sizes, the behavior is the opposite. The fact that the daily mean precipitation is more (or less) smooth in regions with high overall wind is questionable and exceeds the aim of the illustration, but we argue that the model is favoring these covariates to adjust to sharp changes in elevation and wind, as highlighted in Figure 8. By considering the spatial pattern of the smoothness, we argue that

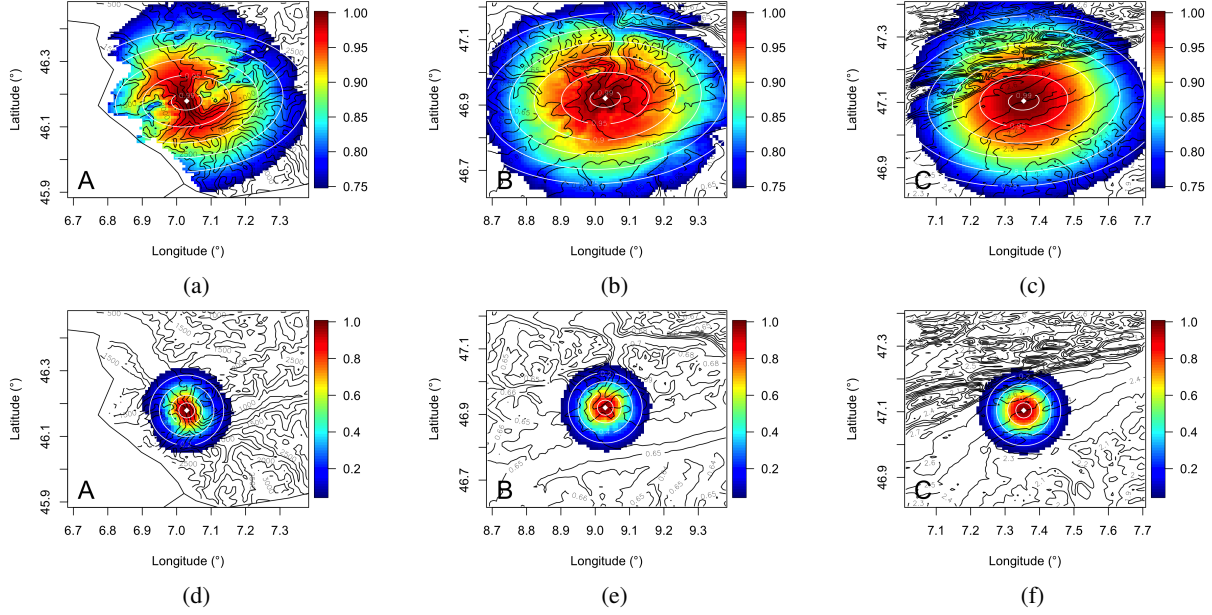


Figure 8: Correlation plots for M-NS (first row) and M-NS-T (second row) at three different regions, with correlation isolines (in white) of M-STAT (first row), and tapered correlation model M-STAT-T (second row). In black, contours with respect to different covariates. Panels (a) and (d) relate to a location in a narrow valley characterized by large wind, surrounded by mountainous territory, with contours describing elevation. In (b) and (e), the contours describe cloud coverage, while in (c) and (f), wind.

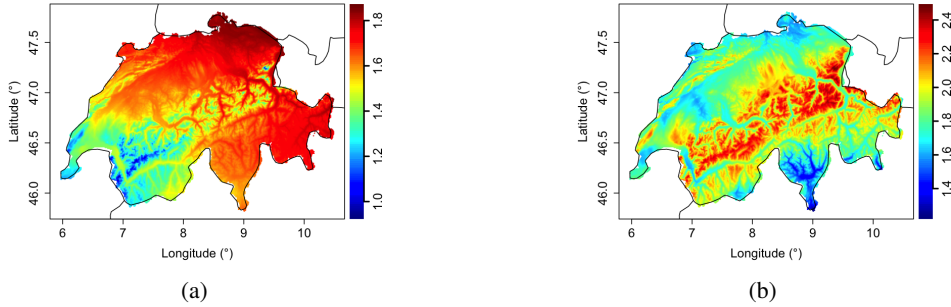


Figure 9: Spatial surfaces of the estimated spatially-varying smoothness for M-NS (left), and M-NS-T (right).

incorporating spatially-varying smoothness is relevant for accurately representing the spatial structure of the process, but as we will see, this does not translate in an increase in prediction capabilities.

A summary of prediction metrics as well as computational, loglikelihood, time and number of parameters is presented in Table 4. The training and test values, as well as the predictive mean and standard for each of the considered models is presented in Appendix 6.2. A first look shows a clear advantage of the nonstationary models in both scenarios but marginal improvement by considering a spatially-varying smoothness, where the advantage of considering a nonstationary model in the smoothness seems to vanish as the sample size increase. M-NS and M-NS-T have lower RMSPE, CRPS, and log-predictive scores than M-STAT and M-STAT-T, respectively, indicating that their predictions are more precise, providing more adequate uncertainty quantifications, and where the worse 5% of the CRPS distributions are nearly half as small as their classical counterparts, meaning more robust uncertainty quantification under a heterogeneous number of holdouts. The improvements in these metrics for M-NS and M-NS-T are substantial, with M-NS showing an approximately 50% reduction compared to M-STAT and a whopping 65% reduction for M-NS-T compared to M-STAT-T. M-NS even matches the performance of M-STAT-T, although the latter has twenty times as many training observations, leading to closer prediction sites.

A first inspection of D_n and the coverage probabilities reveals that M-NS outperforms M-STAT, with more subtle improvements for the Sparse scenario. The coverage of the prediction intervals seems to be sensible to how well the

Table 4: Summary of performance metrics. Standard errors between holdouts are shown in parentheses. Bold text indicates the best metric achieved in each scenario. Time is presented in minutes.

Metric	Dense ($n=500$)			Sparse ($n=10000$)		
	M-STAT	M-NS	M-NS-G	M-STAT-T	M-NS-T	M-NS-T-G
RMSPE	0.074 (0.052)	0.035 (0.020)	0.037 (0.023)	0.032 (0.026)	0.012 (0.013)	0.012 (0.013)
CRPS	0.045 (0.034)	0.020 (0.012)	0.021 (0.014)	0.018 (0.013)	0.005 (0.005)	0.005 (0.005)
$q_{0.95}$ (CRPS)	0.101 (0.080)	0.047 (0.027)	0.051 (0.033)	0.048 (0.043)	0.018 (0.022)	0.018 (0.022)
Log-Score	-1.082 (1.050)	-2.096 (0.572)	-2.024 (0.613)	-2.161 (0.623)	-3.746 (0.694)	-3.744 (0.697)
D_n	0.316 (0.149)	0.268 (0.119)	0.285 (0.122)	0.242 (0.090)	0.213 (0.081)	0.214 (0.081)
CPI	0.883 (0.182)	0.932 (0.085)	0.922 (0.103)	0.934 (0.086)	0.961 (0.048)	0.961 (0.049)
$\dim(\hat{\theta})$	14	24	22	12	27	22
$l_{pen}(\hat{\theta}_{pen})$	-933	-1356	-1336	-37527	-61348	-61319
time	0.64	1.15	0.86	6.58	30.69	21.18

assumption of (4) holds. Regarding the computational time of the optimization routines, it reveals different tradeoff between the Dense and Sparse scenarios. While the nonstationary models in the Dense scenario requires less than an extra minute to offer a flexible representation of the covariance structure, the taper-based models on the other hand requires of up to five times the computational time.

5 Discussion

In this article, we presented a class of parametric modular covariate-based covariance functions that, by leveraging observable spatial covariates, provide a convenient degree of flexibility while offering an economical parameterization, keen to computational efficiency. It allows the representation of up to five sources of nonstationarity, including marginal standard deviation, local geometric anisotropy, and smoothness, all introduced modularly. A tailored regularization parameter fosters well-behaved covariance functions while preserving excellent predictive capabilities. As a special case, the nonstationary model presented in (10) simplifies to a Matérn covariance function and can be adapted for large datasets, enhancing flexibility and computational efficiency for a wide range of sample sizes. Moreover, it offers a plethora of numerical and visual tools to explore the different sources of nonstationarity, allowing, for example, for the identification of misspecification in the trend, as shown in the illustration section.

On a challenging real data example, the nonstationary models produce more meaningful and sensible results than those from a stationary model. The results over one hundred heterogeneous holdouts revealed that the nonstationary models yield better prediction distributions while better honoring the assumption of Gaussian prediction distribution in (4). There is a convenient tradeoff between flexibility and computational efficiency when considering the nonstationary covariance model (10) under moderate sample sizes, yielding a reduction above 50% for RMPSE and CRPS by a tiny added computational cost. This tradeoff is more conservative for taper-based nonstationary models (15), which while achieving better results compared to classic taper-based models, are at the expense of almost five-fold increase over the computational time. This increase stems from the extra calculations required for the sparse semi-distance matrix with elements Q_{ij} at each iteration of the optimization routine, involving computationally intensive routines. Although the computational efficiency gap might be smaller in future versions of the R package *cocons*, the computational requirements may still be prohibitive when handling massive datasets. Three alternative approaches under these scenarios can be to use full-scale approximations (FSAs) combining predictive process methods and covariance tapering [Gyger et al., 2024], to work with multi-resolution approximations (M-RA), allowing local nonstationary covariance functions [Huang et al., 2021], or to consider highly-scalable maximum weighted composite likelihood based on pairs (WCLP) with symmetric weight function based on nearest neighbors [Caamaño-Carrillo et al., 2024].

There was little justification to incorporate an extra spatially-varying smoothness function on top of other spatially-varying models when the goal is to perform predictions. The prediction distributions and the penalized log-likelihood are slightly improved compared to global smoothness nonstationary models. One factor explaining the limited improvement over predictions is the arrangement of spatial locations of the Dense and Sparse scenarios around the prediction locations. While the smoothness parameter concerns the behavior at infinitesimally small distances, most noticeable changes between covariance functions with different smoothness parameters will be at relatively short distances and, with it, where it most influences predictions. This explains the more noticeable improvement in the Dense scenario than in the Sparse scenario, given that for the former the spatial configuration around prediction locations are less populated and at a relative larger distance. Another factor explaining this limited improvement is related to the dataset employed in the illustration, which (although openly accessible) might not be sensible to models representing spatially-varying smoothness since the resulting high-resolution grid of observations is, in fact, solutions of Delaunay linear interpolation

from weather stations, which does not account for the smoothness of the underlying process. Other data sets might be more suitable for benefiting from models with spatially-varying smoothness, such as in Fang and Stein [1998], where the smoothness of longitudinal variations in total column ozone in the Earth’s atmosphere shows a clear dependence on latitude.

While there is a clear improvement over predictions distributions with the presented nonstationary covariance function, the estimation routine demands additional considerations than when employing Gaussian processes with simple stationary covariance models. The initial configuration of the L-BFGS-B numerical optimizer requires specifying boundaries for each of the parameters in the model, which are evaluated during the initial iterations of the algorithm. While setting boundaries that are too wide can lead to non-invertible covariance matrices, narrow boundaries, on the other hand, will oftentimes lead to suboptimal solutions, questioning the validity of results. Moreover, the optimizer often tries to reach an ill-conditioned (relative) maximum, requiring a re-run of the estimation procedure with a larger regularization parameter λ to promote numerical stability. In addition, we have found that sensible different model structures can trigger considerably different solutions for the spatial trend and, with it, the associated residuals, even when the coefficient of the spatially-varying function removed was considerably small. The nonstationary model employed in the illustration for the Dense scenario presents this behavior when simplifying the restricted tilt, which, although close to zero, the reduced model led to a different trend surface, causing an increase of the BIC. This might be closely related to the general challenges of consistently estimating the parameters from a Matérn model within a densely sampled domain [Zhang, 2004]. For M-NS, the square root of the inverse of the approximated Hessian as shown in Appendix 6.3, present values that are sensible larger for the intercept and global standard deviation, scale, and smoothness, which, although these values are considerably smaller when considering taper-based models under larger sample sizes, it suggests that a global level, these parameters are hard to identify.

The spatial model with spatial trend and modular parametric nonstationary covariance function provides a convenient framework for developing model selection approaches involving both sources of nonstationarity. In this setting, there is an added challenge since we also need to address in which source of nonstationarity a covariate should be introduced. Although we have give some intuitions on how a combination of likelihood ratio tests and confidence intervals might be used to address this task, frameworks that perform both estimation and model selection during the optimization routine, such as LASSO or one-step sparse estimation [Chu et al., 2011], are by far more popular and likely computationally more efficient and warrant further investigation.

The model outlined in this paper can be extended in several directions, such as to adequate to spatio-temporal frameworks, to adapt for three-dimensional geostatistical problems such as those found in mining applications, by accounting for an extra source of nonstationarity, or by consider instead a Bayesian framework. Extending to a spatiotemporal framework can range from employing temporally-varying covariates, i.e., covariates of the style $\mathbf{x}(\mathbf{s}, t_i)$, where t_i relates to a specific point in time, including time as an additional covariate; or to employ full geostatistical spatiotemporal approaches, with spatiotemporal covariance matrices [Porcu et al., 2021]. Three-dimensional geostatistical scenarios can be easily implemented by extending the local anisotropic structure to include the extra depth dimension by considering a 3×3 positive definite matrix following the spherical parameterization of covariance matrices [Pinheiro and Bates, 1996]. The model can be extended also considering a spatially-varying nugget effect σ_ϵ^2 present in the noisy version of the process $Z(\cdot)$. This could follow a simple log parameterization such as for the marginal standard deviation parameter $\sigma(\cdot)$, with, for example, an associated parameter ϱ . An application with spatially-varying nugget effect can be found in [Fuglstad et al., 2015]. Lastly, under a frequentist approach, predictions based on (4) do not consider the uncertainty due to parameter estimation. This source of uncertainty might be considerable under low sample sizes or when the number of parameters in the nonstationary model is large relative to the sample size. Under these scenarios, one may opt for Bayesian frameworks instead, which can be easily adapted thanks to the unconstrained centered parameterization.

6 Appendix

6.1 Positive definiteness of the presented modular covariance function

In this appendix, we show that the nonstationary covariance function as in (6), with $\nu(\mathbf{s}_i, \mathbf{s}_j; \boldsymbol{\xi}) = \sqrt{\nu_i \nu_j}$, where $\nu_i = \nu(\mathbf{s}_i; \boldsymbol{\xi})$ follows (9) is positive definite. The proof is a simple extension of [Anderes and Stein, 2011], which shows that the covariance function (6), with spatially-varying smoothness $\nu(\mathbf{s}_i, \mathbf{s}_j; \boldsymbol{\xi}) = (\nu_i + \nu_j)/2$ is positive definite. We start by introducing the lemma by [Anderes and Stein, 2011], which is then used to show positive definiteness on the introduced covariance function (6) with $\nu(\mathbf{s}_i, \mathbf{s}_j; \boldsymbol{\xi}) = \sqrt{\nu_i \nu_j}$, where $\nu_i = \nu(\mathbf{s}_i; \boldsymbol{\xi})$ follows (9).

Lemma 1. Let $\Sigma(\cdot; \mathbf{x}) : \mathbb{R}^p \rightarrow d \times d$ real positive-definite matrices, $\sigma(\cdot; \mathbf{x}) : \mathbb{R}^p \rightarrow \mathbb{R}$, and for each $\mathbf{x} \in \mathbb{R}^p$, $g(\cdot; \mathbf{x}) \in L^2(dH)$, being H nonnegative and bounded on $[0, \infty)$. Then

$$\mathcal{C}(\mathbf{s}_i, \mathbf{s}_j) = \sigma_i \sigma_j \frac{|\Sigma_i|^{1/4} |\Sigma_j|^{1/4}}{|\frac{\Sigma_i + \Sigma_j}{2}|^{1/2}} \int_0^\infty \exp(-Q_{ij}w) g(w; \mathbf{x}_i) g(w; \mathbf{x}_j) dH(w) \quad (20)$$

is positive definite. By taking $dH(w) = w^{-1} \exp(-1/4w) dw$ with respect to Lebesgue measure, $g(w; \mathbf{x}) = w^{-\nu(\mathbf{x})/2}$, by using a convolution argument from (Paciorek [2003], p.23), and by using (3.471.9) in Gradshteyn and Ryzhik [2014] it can be shown the resulting covariance function is positive definite and leads to (6) with $\nu_{ij} = (\nu_i + \nu_j)/2$ (Stein [2005], p.3).

Claim. The covariance function (6) with $\nu(\mathbf{s}_i, \mathbf{s}_j; \xi) = \sqrt{\nu_i \nu_j}$, where $\nu_\ell = \nu(\mathbf{x}_\ell; \xi)$, is defined as in (9) being $\nu_{\min} \leq \nu_\ell \leq \nu_{\max}$ leading to

$$\mathcal{C}_R(\mathbf{x}_i, \mathbf{x}_j) = \sigma_i \sigma_j \frac{|\Sigma_i|^{1/4} |\Sigma_j|^{1/4}}{|\frac{\Sigma_i + \Sigma_j}{2}|^{1/2}} \int_0^\infty \exp(-Q_{ij}w) h(w; \mathbf{x}_i, \mathbf{x}_j) dH(w), \quad (21)$$

with $h(w; \mathbf{x}_i, \mathbf{x}_j) = w^{-\sqrt{\nu_i \nu_j}}$, is positive definite.

Proof. We define the piecewise function

$$m(w; \mathbf{x}) = \begin{cases} w^{-\frac{\nu_{\min}}{2}}, & \text{if } w \leq 1 \\ w^{-\frac{\nu_{\max}}{2}}, & \text{o.w.} \end{cases},$$

which for each \mathbf{x} , $m(\cdot; \mathbf{x}) \in L^2(dH)$. Notice then that $h(w; \mathbf{x}_i, \mathbf{x}_j) \geq m(w; \mathbf{x}_i) m(w; \mathbf{x}_j)$, $\forall w \in \mathbb{R}^+$. Then, using the convolution argument (Paciorek [2003], p. 27),

$$\begin{aligned} \sum_{i=1}^n \sum_{j=1}^n c_i c_j \mathcal{C}_R(\mathbf{s}_i, \mathbf{s}_j) &= \sum_{i=1}^n \sum_{j=1}^n c_i c_j \sigma_i \sigma_j \frac{|\Sigma_i|^{1/4} |\Sigma_j|^{1/4}}{|\frac{\Sigma_i + \Sigma_j}{2}|^{1/2}} \int_0^\infty \exp(-Q_{ij}w) h(w; \mathbf{x}_i, \mathbf{x}_j) dH(w) \\ &\geq \sum_{i=1}^n \sum_{j=1}^n c_i c_j \sigma_i \sigma_j \frac{|\Sigma_i|^{1/4} |\Sigma_j|^{1/4}}{|\frac{\Sigma_i + \Sigma_j}{2}|^{1/2}} \int_0^\infty \exp(-Q_{ij}w) m(w; \mathbf{x}_i) m(w; \mathbf{x}_j) dH(w) \\ &= (2\sqrt{\pi})^{d/2} \sum_{i=1}^n \sum_{j=1}^n c_i c_j \sigma_i \sigma_j |\Sigma_i|^{1/4} |\Sigma_j|^{1/4} \int_0^\infty \left(\int_{\mathcal{D}} K_{\mathbf{s}_i}(\mathbf{u}) K_{\mathbf{s}_j}(\mathbf{u}) d\mathbf{u} \right) m(w; \mathbf{x}_i) m(w; \mathbf{x}_j) dH(w) \\ &= (2\sqrt{\pi})^{d/2} \int_0^\infty \int_{\mathcal{D}} \left(\sum_{i=1}^n c_i \sigma_i |\Sigma_i|^{1/4} K_{\mathbf{s}_i}(\mathbf{u}) m(w; \mathbf{x}_i) \right)^2 d\mathbf{u} dH(w) \geq 0 \end{aligned}$$

which is nonnegative, proving that $\mathcal{C}_R(\mathbf{s}_i, \mathbf{s}_j)$ assign nonnegative values to all quadratics forms. Then, by using the convolution argument from (Paciorek [2003], p.23), and by using (3.471.9) in Gradshteyn and Ryzhik [2014] it can be shown the resulting positive definite covariance function leads to

$$\mathcal{C}_R(\mathbf{x}_i, \mathbf{x}_j) = \sigma_i \sigma_j \frac{|\Sigma_i|^{1/4} |\Sigma_j|^{1/4}}{|\frac{\Sigma_i + \Sigma_j}{2}|^{1/2}} \mathcal{M}_{\sqrt{\nu_i \nu_j}} \left(\sqrt{Q_{ij}} \right) \quad (22)$$

□

6.2 Illustration figures

The following Figures provided added information to the illustration section.

6.3 Numerical summary of nonstationary models

The following tables present parameter estimates for M-NS and M-NS-T from the illustration section.

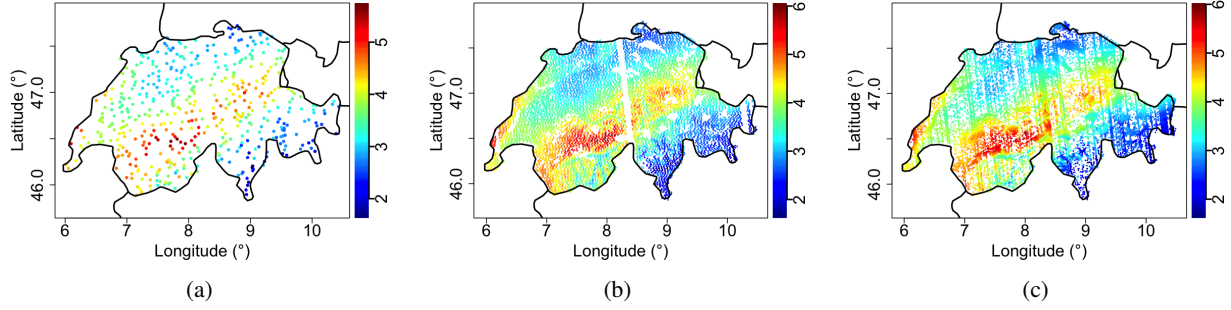


Figure 10: Precipitation under the training Dense (a) and Sparse (b) datasets, and test dataset (c).

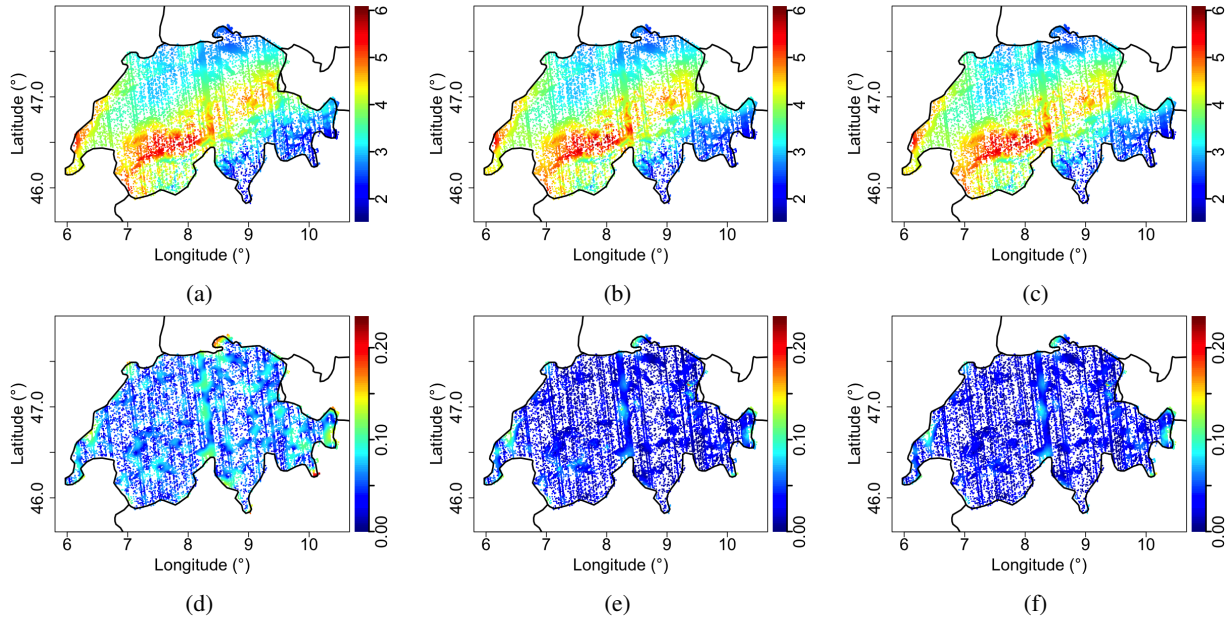


Figure 11: Predictive means and standard deviations for M-STAT (first column), M-NS (second column), and M-NS-G (third column).

Table 5: Parameter estimates for the dense model M-NS. Where available, standard error estimates are given in parentheses. Slots where a (–) is present mean that the covariate was not considered in the final model.

covariate	trend	var	scale	aniso	tilt	smooth
intercept	3.705 (0.150)	-0.733 (0.217)	0.302 (0.074)	-0.118 (0.061)	0.036 (0.067)	1.044 (0.246)
wind	-0.289 (0.046)	–	–	–	–	–
merwind	0.100 (0.041)	–	–	–	–	–
BI004	0.091 (0.042)	–	–	–	–	–
BI015	-0.464 (0.024)	–	–	–	–	–
cloud	0.066 (0.037)	–	–	–	–	–
elev	0.039 (0.014)	–	–	–	–	–
lati	-0.206 (0.094)	–	–	–	–	–
long	-0.194 (0.086)	–	–	–	–	–
log(cloud)	–	0.396 (0.061)	–	–	-0.041 (0.041)	–
log(wind)	–	-0.345 (0.076)	-0.100 (0.020)	–	–	0.441 (0.155)
log(elev)	–	0.028 (0.053)	0.048 (0.013)	–	–	–
log(lati)	–	–	–	0.072 (0.052)	–	–
log(long)	–	–	–	-0.112 (0.048)	–	0.532 (0.146)

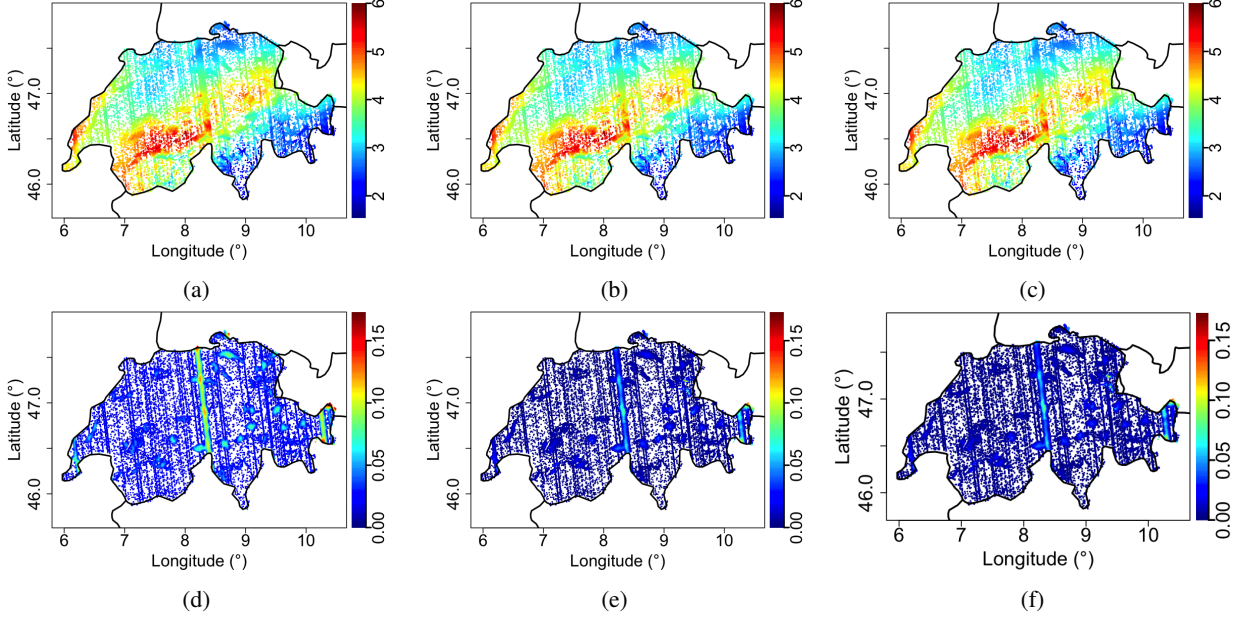


Figure 12: Predictive means and standard deviations for M-STAT-T (first column), M-NS-T (second column), and M-NS-T-G (third column).

Table 6: Parameter estimates for the sparse model M-NS-T. Where available, the square root of the inverse of the Hessian is given in parentheses. Slots where a (–) is present mean that the covariate was not considered in the final model.

covariate	trend	var	scale	smooth
intercept	3.704 (0.007)	-4.068 (0.016)	-0.013 (0.033)	0.916 (0.171)
wind	-0.395 (0.006)	–	–	–
merwind	0.093 (0.007)	–	–	–
BI004	-0.011 (0.007)	–	–	–
BI015	-0.493 (0.004)	–	–	–
ccloud	-0.017 (0.007)	–	–	–
elev	0.001 (0.001)	–	–	–
lati	-0.129 (0.007)	–	–	–
long	-0.259 (0.007)	–	–	–
log(ccloud)	–	0.536 (0.015)	-0.073 (0.011)	0.229 (0.169)
log(elev)	–	-0.007 (0.003)	-0.013 (0.002)	0.012 (0.165)
log(wind)	–	-0.257 (0.012)	0.445 (0.008)	-0.854 (0.255)
log(lati)	–	-0.389 (0.020)	-0.262 (0.041)	0.423 (0.221)
log(long)	–	0.178 (0.016)	0.259 (0.036)	-0.259 (0.175)

6.4 Correlation functions with compact support

$$\text{Spherical: } \rho(h; \delta) = I_{\{h < \delta\}} \left(1 - \frac{3h}{2\delta} + \frac{1}{2} \frac{h^3}{\delta^3} \right),$$

$$\text{Wendland}_1: \rho(h; \delta) = I_{\{h < \delta\}} \left(1 - \frac{h}{\delta} \right)^4 \left(\frac{4h}{\delta} + 1 \right),$$

$$\text{Wendland}_2: \rho(h; \delta) = I_{\{h < \delta\}} \left(1 - \frac{h}{\delta} \right)^6 \left(\frac{35}{3} \frac{h^2}{\delta^2} + 6 \frac{h}{\delta} + 1 \right),$$

where $\delta > 0$.

6.5 Details for accessing the dataset in Section 4

The employed dataset is openly available via the web interface <https://cds.climate.copernicus.eu/cdsapp#!/dataset/sis-biodiversity-era5-regional?tab=overview>. It requires login credentials (non-academic credentials work as well). Steps to download the intended dataset, as well as the preprocessing to select these covariates from Switzerland, and to retrieve elevation information, are available in the Git repository in 6.7.

6.6 Computational resources

For the illustration and simulation studies, we used a Macbook Air M2 with 16Gb of memory RAM with macOS Sonoma 14.3.0.

6.7 Source files

R source files are available in the git repository <https://github.com/blasif/j.envIRON.2024>. The README.txt file gives an overview of the available files as well as how to run them.

CRedit author statement

Federico Blasi: Conceptualization, Methodology, Software, Formal Analysis, Data Curation, Writing - Original Draft, Writing - Review & Editing, Visualization, **Reinhard Furrer**: Supervision, Writing - Review & Editing.

Acknowledgments

This work is supported by the Swiss National Science Foundation SNSF-175529.

References

- M. Abramowitz and I. A. Stegun, editors. *Handbook of Mathematical Functions*. Dover, New York, 1970.
- Hirotougu Akaike. Information theory and an extension of the maximum likelihood principle. *Selected papers of hirotugu akaike*, pages 199–213, 1998.
- Ethan B Anderes and Michael L Stein. Local likelihood estimation for nonstationary random fields. *Journal of Multivariate Analysis*, 102(3):506–520, 2011.
- Ioannis Andrianakis and Peter G Challenor. The effect of the nugget on gaussian process emulators of computer models. *Computational Statistics & Data Analysis*, 56(12):4215–4228, 2012.
- Sudipto Banerjee and AE Gelfand. On smoothness properties of spatial processes. *Journal of Multivariate Analysis*, 84(1):85–100, 2003.
- Subhasish Basak, Sébastien Petit, Julien Bect, and Emmanuel Vazquez. Numerical issues in maximum likelihood parameter estimation for gaussian process interpolation. In *International Conference on Machine Learning, Optimization, and Data Science*, pages 116–131. Springer, 2021.
- Moreno Bevilacqua, Tarik Faouzi, Reinhard Furrer, and Emilio Porcu. Estimation and prediction using generalized wendland covariance functions under fixed domain asymptotics. *The Annals of Statistics*, 47(2):828–856, 2019.
- Federico Blasi. *cocons: Covariate-based Covariance Functions For nonstationary Gaussian Processes*, 2024. URL <https://github.com/blasif/cocons/>. R package version 0.1.
- Federico Blasi, Christian Caamaño-Carrillo, Moreno Bevilacqua, and Reinhard Furrer. A selective view of climatological data and likelihood estimation. *Spatial Statistics*, 50:100596, 2022.
- Luke Bornn, Gavin Shaddick, and James V Zidek. Modeling nonstationary processes through dimension expansion. *Journal of the American statistical association*, 107(497):281–289, 2012.
- Christian Caamaño-Carrillo, Moreno Bevilacqua, Cristian López, and Víctor Morales-Oñate. Nearest neighbors weighted composite likelihood based on pairs for (non-) gaussian massive spatial data with an application to tukey-hh random fields estimation. *Computational Statistics & Data Analysis*, 191:107887, 2024.
- Catherine A Calder. A dynamic process convolution approach to modeling ambient particulate matter concentrations. *Environmetrics: The official journal of the International Environmetrics Society*, 19(1):39–48, 2008.

- Jiawen Chen, Wancen Mu, Yun Li, and Didong Li. On the identifiability and interpretability of gaussian process models. *Advances in Neural Information Processing Systems*, 36, 2024.
- Tingjin Chu, Jun Zhu, and Haonan Wang. Penalized maximum likelihood estimation and variable selection in geostatistics. *Annals of statistics*, 39(5):2607–2625, 2011.
- Daniel Cooley, Douglas Nychka, and Philippe Naveau. Bayesian spatial modeling of extreme precipitation return levels. *Journal of the American Statistical Association*, 102(479):824–840, 2007.
- Victor De Oliveira and Zifei Han. On information about covariance parameters in gaussian matern random fields. *Journal of Agricultural, Biological and Environmental Statistics*, 27(4):690–712, 2022.
- Dongping Fang and Michael L Stein. Some statistical methods for analyzing the toms data. *Journal of Geophysical Research: Atmospheres*, 103(D20):26165–26182, 1998.
- Francky Fouedjio. Second-order non-stationary modeling approaches for univariate geostatistical data. *Stochastic Environmental Research and Risk Assessment*, 31(8):1887–1906, 2017.
- Montserrat Fuentes. A high frequency kriging approach for non-stationary environmental processes. *Environmetrics: The official journal of the International Environmetrics Society*, 12(5):469–483, 2001.
- Montserrat Fuentes. Spectral methods for nonstationary spatial processes. *Biometrika*, 89(1):197–210, 2002.
- Geir-Arne Fuglstad, Daniel Simpson, Finn Lindgren, and Håvard Rue. Does non-stationary spatial data always require non-stationary random fields? *Spatial Statistics*, 14:505–531, 2015.
- Reinhard Furrer, Marc G Genton, and Douglas Nychka. Covariance tapering for interpolation of large spatial datasets. *Journal of Computational and Graphical Statistics*, 15(3):502–523, 2006.
- Alan E Gelfand, Peter Diggle, Peter Guttorp, and Montserrat Fuentes. *Handbook of spatial statistics*. CRC press, 2010.
- Owais Gilani, Veronica J Berrocal, and Stuart A Batterman. Non-stationary spatio-temporal modeling of traffic-related pollutants in near-road environments. *Spatial and spatio-temporal epidemiology*, 18:24–37, 2016.
- Tilmann Gneiting and Adrian E Raftery. Strictly proper scoring rules, prediction, and estimation. *Journal of the American statistical Association*, 102(477):359–378, 2007.
- Izrail Solomonovich Gradshteyn and Iosif Moiseevich Ryzhik. *Table of integrals, series, and products*. Academic press, 2014.
- Tim Gyger, Reinhard Furrer, and Fabio Sigrüst. Iterative methods for full-scale gaussian process approximations for large spatial data. *arXiv preprint arXiv:2405.14492*, 2024.
- Dave Higdon, Jenise Swall, and John Kern. Non-stationary spatial modeling. *Bayesian statistics*, 6(1):761–768, 1999.
- David Higdon. A process-convolution approach to modelling temperatures in the north atlantic ocean. *Environmental and Ecological Statistics*, 5(2):173–190, 1998.
- Jay M Ver Hoef, Erin Peterson, and David Theobald. Spatial statistical models that use flow and stream distance. *Environmental and Ecological statistics*, 13(4):449–464, 2006.
- Peter D Hoff and Xiaoyue Niu. A covariance regression model. *Statistica Sinica*, pages 729–753, 2012.
- Jeffrey Hollister, Tarak Shah, Alec L. Robitaille, Marcus W. Beck, and Mike Johnson. *elevatr: Access Elevation Data from Various APIs*, 2021. URL <https://github.com/jhollist/elevatr/>. R package version 0.4.2.
- Huang Huang, Lewis R Blake, Matthias Katzfuss, and Dorit M Hammerling. Nonstationary spatial modeling of massive global satellite data. *arXiv preprint arXiv:2111.13428*, 2021.
- Finn Lindgren, Håvard Rue, and Johan Lindström. An explicit link between gaussian fields and gaussian markov random fields: the stochastic partial differential equation approach. *Journal of the Royal Statistical Society: Series B (Statistical Methodology)*, 73(4):423–498, 2011.
- Kanti V Mardia and Roger J Marshall. Maximum likelihood estimation of models for residual covariance in spatial regression. *Biometrika*, 71(1):135–146, 1984.
- Bertil Matérn. *Spatial variation*, volume 36. Springer Science & Business Media, 2013.
- Joaquim Henriques Vianna Neto, Alexandra M Schmidt, and Peter Guttorp. Accounting for spatially varying directional effects in spatial covariance structures. *Journal of the Royal Statistical Society: Series C (Applied Statistics)*, 63(1):103–122, 2014.
- Christopher J Paciorek and Mark J Schervish. Spatial modelling using a new class of nonstationary covariance functions. *Environmetrics: The official journal of the International Environmetrics Society*, 17(5):483–506, 2006.

- Christopher Joseph Paciorek. *Nonstationary Gaussian processes for regression and spatial modelling*. PhD thesis, Carnegie Mellon University, 2003.
- Chien-Yu Peng and CF Jeff Wu. On the choice of nugget in kriging modeling for deterministic computer experiments. *Journal of Computational and Graphical Statistics*, 23(1):151–168, 2014.
- José C Pinheiro and Douglas M Bates. Unconstrained parametrizations for variance-covariance matrices. *Statistics and computing*, 6(3):289–296, 1996.
- Emilio Porcu, Reinhard Furrer, and Douglas Nychka. 30 years of space–time covariance functions. *Wiley Interdisciplinary Reviews: Computational Statistics*, 13(2):e1512, 2021.
- Emilio Porcu, Moreno Bevilacqua, Robert Schaback, and Chris J Oates. The mat\`ern model: A journey through statistics, numerical analysis and machine learning. *arXiv preprint arXiv:2303.02759*, 2023.
- Brian J Reich, Jo Eidsvik, Michele Guindani, Amy J Nail, and Alexandra M Schmidt. A class of covariate-dependent spatiotemporal covariance functions. *The annals of applied statistics*, 5(4):2265, 2011.
- Mark D Risser and Catherine A Calder. Regression-based covariance functions for nonstationary spatial modeling. *Environmetrics*, 26(4):284–297, 2015.
- Paul D Sampson and Peter Guttorp. Nonparametric estimation of nonstationary spatial covariance structure. *Journal of the American Statistical Association*, 87(417):108–119, 1992.
- Alexandra M Schmidt and Peter Guttorp. Flexible spatial covariance functions. *Spatial Statistics*, 37:100416, 2020.
- Alexandra M Schmidt, Peter Guttorp, and Anthony O’Hagan. Considering covariates in the covariance structure of spatial processes. *Environmetrics*, 22(4):487–500, 2011.
- Isaac J Schoenberg. Metric spaces and completely monotone functions. *Annals of Mathematics*, pages 811–841, 1938.
- Michael L Stein. *Interpolation of spatial data: some theory for kriging*. Springer Science & Business Media, 1999.
- Michael L Stein. Nonstationary spatial covariance functions. *Unpublished technical report*, 2005.
- H Wouters. Downscaled bioclimatic indicators for selected regions from 1979 to 2018 derived from reanalysis. *Copernicus Climate Change Service (C3S) Climate Data Store (CDS)*, 2021.
- Hao Xu and Paolo Gardoni. Improved latent space approach for modelling non-stationary spatial–temporal random fields. *Spatial Statistics*, 23:160–181, 2018.
- Andrew Zammit-Mangion, Tin Lok James Ng, Quan Vu, and Maurizio Filippone. Deep compositional spatial models. *Journal of the American Statistical Association*, pages 1–22, 2021.
- Hao Zhang. Inconsistent estimation and asymptotically equal interpolations in model-based geostatistics. *Journal of the American Statistical Association*, 99(465):250–261, 2004.